

# An Information Potential Approach to Integrated Sensor Path Planning and Control

Wenjie Lu, Guoxian Zhang, and Silvia Ferrari, *Senior Member, IEEE*

**Abstract**—This paper presents an information potential method for integrated path planning and control. The method is applicable to unicycle robotic sensors deployed to classify multiple targets in an obstacle-populated environment. A new navigation function, referred to as information potential, is generated from the target conditional mutual information, and used to design a closed-loop stable switched control law. The information potential is shown to obey the properties of potential navigation functions and to enable measurements that maximize the information value over time. The information potential is also used to construct a local roadmap for escaping local minima. The properties and computational complexity of the local roadmap algorithm are analyzed. Numerical simulation results show that the method outperforms other strategies, such as rapidly exploring random trees and classical potential field methods.

**Index Terms**—Demining systems, information value, mutual information, robot path planning, sensor networks.

## I. INTRODUCTION

THIS paper addresses the problem of integrated path planning and control for a robotic sensor used to classify multiple targets in an environment populated with obstacles and other mobile sensors. This problem, which is also known as a treasure hunt, is relevant to many mobile sensor applications such as mine hunting [1], cleaning [2], and monitoring of urban environments [3] and manufacturing plants [4]. Diffeomorphism models have been recently developed to learn the kinematics of robotic sensors and actuators, and their environment, and to recover nonlinear sensing phenomena with bounded field-of-views (FOVs) [5]. However, most of the existing path-planning methods are not designed to take into account such models of environmental uncertainty and sensor measurements. Furthermore, they cannot be easily modified to account for the geometries of the targets and sensor FOV, while also performing online obstacle detection and avoidance.

Methods based on cell decomposition [6], probabilistic roadmaps (PRMs) [18], and rapidly exploring random trees

(RRTs) [7]–[9] have been proposed for planning the path of robotic sensors based on the target geometry, or on the posterior probability of a target state. These methods, however, can produce paths that are infeasible under realistic dynamic constraints and cannot be efficiently implemented when obstacles are detected online. Information-driven sensor planning methods have been recently proposed to make use of information-theoretic functions for assessing the value of sensor measurements, and to decide the best sensor mode or measurement sequence [10]–[12]. A maximum-likelihood solution to the problem of calibrating the parameters of exteroceptive sensors was proposed in [13]. A proportion-integral average consensus estimator was developed in [14] and used for the control of mobile sensors in decentralized environmental modeling. Hierarchical approaches have been developed to generate optimal sensing actions or subtasks given the posterior probability of a target state obtained through Bayesian inference [15], [16]. Although these methods do not take into account the sensor FOV and target geometries, they have been proven very effective at planning sensor decisions based on probabilistic models of the measurement process that can account for environmental uncertainty and prior information.

An information potential (IP) approach is presented for generating a potential navigation function and roadmap based on a probabilistic model of the measurement process and on the geometries of targets and sensor FOV. The potential navigation function, based on mutual information, is used to develop a switched feedback control law for integrated sensor path planning and control. Mutual information is a measure of the information content of one random variable about another random variable. It has been previously used for sensor planning in multitarget detection, classification, and feature inference [6], [17]. In this paper, the target information value is represented by a conditional mutual information function developed in [18]. Although other information-theoretic functions have been proposed for sensor planning [19], conditional mutual information is chosen here because it is additive, symmetric, nonmyopic, and always nonnegative. Based on these characteristics, the IP function can be shown to obey the properties of potential navigation functions and results in a control law that is closed-loop stable.

Although many potential navigation functions have been developed for robot motion planning, they are not applicable to sensor path planning because they do not take into account the geometries of the targets and sensor FOV and do not consider the target information value [20]–[24]. In addition, while classical potential field (PF) methods are well suited to online motion planning and stability analysis, their effectiveness can be limited

Manuscript received September 17, 2013; accepted March 17, 2014. Date of publication June 16, 2014; date of current version August 4, 2014. This paper was recommended for publication by Associate Editor T. Hamel and Editor D. Fox upon evaluation of the reviewers' comments. This work was supported by the National Science Foundation under Grant ECCS 1028506.

W. Lu and S. Ferrari are with the Department of Mechanical Engineering and Materials Science, Duke University, Durham, NC 27708 USA (e-mail: wjlu99@gmail.com; sferrari@duke.edu).

G. Zhang was with the Department of Mechanical Engineering and Materials Science, Duke University, Durham, NC 27708 USA. He is now with Groupon, Inc., Palo Alto, CA 94306 USA (e-mail: zhangguoxian@gmail.com).

Color versions of one or more of the figures in this paper are available online at <http://ieeexplore.ieee.org>.

Digital Object Identifier 10.1109/TRO.2014.2312812

by trapping in local minima, goals nonreachable with obstacles nearby, stabilization, and inability to enter narrow passages [25]. All of these issues are exacerbated by the presence of targets due to a higher density of local minima and to the difficulty of reaching and stabilizing the robot in a C-target region in the presence of no-slip constraints. Besides compromising robot navigation, these issues can significantly decrease classification performance, especially when important targets are located near obstacles, local minima, or in narrow passages. One approach to stabilizing nonholonomic systems has been to use time-varying smooth control laws [26]–[28], while another has been to use discontinuous feedback control [29]. In this paper, a switched control approach based on switched potentials [30] is used to integrate sensor path planning with dynamic feedback control. As a result, the switched control law can be proven asymptotically stable and guaranteed to converge to the target of highest information value.

An effective approach for escaping local minima is to follow a new local path generated through a random-walk algorithm. Another approach is to construct a PF without any local minima via Morse (or harmonic) functions [31]–[34]. In the IP method, the same IP function used to derive the switched control law is utilized to build a local roadmap for escaping local minima. Thus, the connectivity between milestones can be verified *a priori*, and the robotic sensor is proven to asymptotically converge to the milestone with the lowest potential (or highest information value). The simulation results show that the IP-controlled robotic sensor is capable of obtaining measurements from the most valuable targets, entering narrow passages, and escaping local minima, while avoiding obstacles online. As a result, the IP method leads to significant improvements in classification performance and sensor efficiency compared with existing RRT and PF methodologies.

## II. PROBLEM FORMULATION AND ASSUMPTIONS

This paper considers the problem of integrated navigation and control for a robotic sensor deployed to classify multiple targets in an obstacle-populated environment. The robotic sensor consists of an unmanned ground vehicle equipped with an on-board sensor and with autonomous computing and wireless communication capabilities. Let the vehicle geometry be described by a rigid object  $\mathcal{A}$  that is a compact subset of a workspace  $\mathcal{W} \subset \mathbb{R}^3$ .  $\mathcal{W}$  is populated by  $N$  rigid obstacles  $\mathcal{B}_1, \dots, \mathcal{B}_N$  and  $M$  fixed and rigid targets  $\mathcal{T}_1, \dots, \mathcal{T}_M$ . It is assumed that all targets and obstacles are closed subsets of  $\mathcal{W}$  and that the set of targets is selected by a target-assignment algorithm and represented by an index set  $I_T$ . Every target  $\mathcal{T}_i$ , with  $i \in I_T$ , is characterized by a discrete random state variable  $X$ , with an unknown constant value  $x_i$  to be inferred or *classified* by the robotic sensor. As schematized in Fig. 1, the sensor FOV, which is denoted by  $\mathcal{S} \subset \mathbb{R}^3$ , is defined as a compact subset of  $\mathcal{W}$  from which the robot can obtain sensor measurements.

Let  $\mathcal{F}_W$  denote a fixed Cartesian frame, with origin  $O_W$ , embedded in  $\mathcal{W}$ , and  $\mathcal{F}_A$  denote a moving Cartesian frame, with origin  $O_A$ , embedded in  $\mathcal{A}$ . Assuming  $\mathcal{A}$  and  $\mathcal{S}$  are both rigid, and  $\mathcal{S}$  is fixed with respect to  $\mathcal{A}$ , the robot configuration  $\mathbf{q} =$

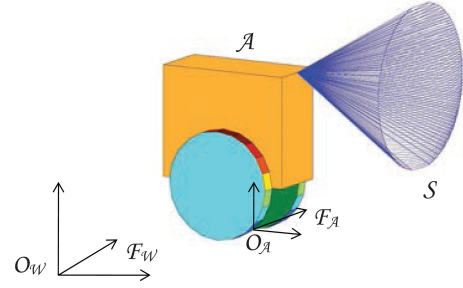


Fig. 1. Robotic sensor with vehicle geometry  $\mathcal{A}$  and sensor FOV  $\mathcal{S}$ .

$[x \ y \ \theta]^T$  can be used to specify the position and orientation of every point in  $\mathcal{A}$ , and every point in  $\mathcal{S}$ , with respect to  $\mathcal{F}_W$ , where  $x$ ,  $y$ , and  $\theta$  are the coordinates and orientation of  $\mathcal{F}_A$  with respect to  $\mathcal{F}_W$ . Let  $\mathcal{C}$  denote the configuration space and  $\mathcal{A}(\mathbf{q})$  denote the subset of  $\mathcal{W}$  occupied by  $\mathcal{A}$  at configuration  $\mathbf{q}$ . Then, the subset of  $\mathcal{W}$  occupied by  $\mathcal{S}$  at configuration  $\mathbf{q}$  can be denoted by  $\mathcal{S}(\mathbf{q})$  and used to represent the set of all points in  $\mathcal{W}$  that can be measured by the on-board sensor when the robot is at  $\mathbf{q}$ . It follows that the robotic sensor can obtain measurements  $z_i$  from a target  $\mathcal{T}_i$  iff  $\mathcal{T}_i \cap \mathcal{S}(\mathbf{q}) \neq \emptyset$ .

The configuration vector  $\mathbf{q}$  must also satisfy the robot dynamic equation which, in this paper, is given by the unicycle model in 4-D phase space [35]

$$\dot{\chi} = \begin{bmatrix} \dot{x} \\ \dot{y} \\ \dot{\theta} \\ \dot{v} \end{bmatrix} = \begin{bmatrix} v \cos \theta \\ v \sin \theta \\ w \\ a \end{bmatrix} = \mathbf{f}(\chi, \mathbf{u}) \quad (1)$$

where  $\chi \in \mathbb{R}^4$  is the robot state,  $v$  is the linear velocity,  $w$  is the angular velocity, and  $a$  is the linear acceleration. The robot control vector is  $\mathbf{u} = [u_1 \ u_2]^T = [a \ w]^T \in \mathcal{U} \subset \mathbb{R}^2$ , where  $\mathcal{U}$  represents the space of admissible control inputs. Although a double-integrator model for (1) can be used for position-based planning and control [34], this approach is not applicable to configuration-based planning and control [35]. Thus, a switched control law defined in a 3-D configuration space is presented in Section III-B.

The target state  $X$ , the sensor measurement  $Z$ , and the sensor parameter or environmental condition  $E$  are assumed to be discrete random variables. If  $x_i$  is any possible value of  $X$ , the probability mass of  $x_i$ , denoted by  $p_X(x_i)$ , is the probability of the event  $\{X = x_i\}$  or  $\mathbf{P}(\{X = x_i\})$ . Let upper case italic characters denote random variables and lower case italic characters denote real numbers. Then, the measurement process can be described by a joint probability mass function (PMF) that, typically, can be factorized as follows

$$p_{X,Z,E}(x_i, z_i, e_i) = p_{Z|X,E}(z_i | x_i, e_i) p_X(x_i) p_E(e_i) \quad (2)$$

because  $X$  and  $E$  are independent random variables. The conditional PMF  $p_{Z|X,E}$  is obtained from the physical principles underlying the measurement process. The PMFs  $p_X$  and  $p_E$ , known as *priors*, are computed from prior environmental information when available, or are otherwise assumed to be uniformly distributed. The probabilistic model in (2) can also be

extended to multiple state variables [36] and continuous random variables [37]. Various sensors have been modeled by (2), either from first principles or real data [36], [38].

A sensor measurement  $z_i$  is obtained when the sensor FOV intersects the  $i$ th target geometry and is represented by the event  $\{Z = z_i | \mathcal{T}_i \cap \mathcal{S}(\mathbf{q}) \neq \emptyset, E = e_i\}$ , where  $e_i$  is assumed known for simplicity. The posterior PMF of the  $i$ th target state can be obtained from the measurement model (2) and Bayes' rule

$$p_{X|Z,E}(x_i | z_i, e_i) = \frac{p_{Z|X,E}(z_i | x_i, e_i)p_X(x_i)}{\sum_{x_i} p_{Z|X,E}(z_i | x_i, e_i)p_X(x_i)} \quad (3)$$

for  $i = 1, \dots, M$ , since (2) holds for all targets. Then, the target can be classified according to the conditional expectation

$$\hat{x}_i \triangleq \mathbb{E}_X[X | Z = z_i, E = e_i] = \sum_{x_i} x_i p_{X|Z,E}(x_i | z_i, e_i) \quad (4)$$

and is considered to be correctly classified when  $\hat{x}_i = x_i$ , where  $x_i$  is the true target state value.

The problem considered in this paper is to plan the path and control for the robotic sensor in (1), such that (I) the number of targets correctly classified is maximized, and (II) collisions with all obstacles are avoided. This problem is motivated by security and reconnaissance applications in which an *in-situ* robotic sensor is deployed to classify targets after they have been detected and localized based on environmental maps and remote sensor measurements. Thus, it is assumed that at the initial time  $t_0$ , the robotic sensor has no knowledge of the obstacles, which may be fixed or moving in  $\mathcal{W}$ . When a new obstacle is *detected* at a time  $t > t_0$ , its geometry and location are assumed to become known without error. Targets differ from the obstacles in that they are fixed in  $\mathcal{W}$ , and while their classification is unknown *a priori*, their geometries and locations are assumed known at  $t_0$ . In order to reduce the algorithm complexity, it is also assumed that  $\mathcal{A}$  is a right prism with the base face adjacent to the  $xy$ -plane, and  $\mathcal{S}$  is a 3-D cone. Obstacles and targets are assumed to be right prisms with the base face parallel to the  $xy$ -plane. The next section presents an IP integrated path planning and control method that achieves control objectives (I) and (II) mentioned above, and guarantees asymptotic closed-loop stability for the robotic sensor in (1).

### III. INFORMATION POTENTIAL METHOD

Information-driven sensor planning utilizes information-theoretic functions to assess the value of a set of sensor measurements and to decide the best sensor mode or measurement sequence [11], [12]. Because target classification can be reduced to the problem of estimating one or more random variables from partial or imperfect measurements, the value of future measurements may be represented by their expected information value. Information-theoretic functions, such as information entropy, have been proposed to assess the information value of sensor measurements [19], [37]. This paper presents an approach for building a potential navigation function and roadmap based on the information value and geometry of the targets, referred to as the IP method. The approach uses a novel IP function, which is presented in Section III-A, to develop a switched feedback

control law for integrated sensor path planning and control (see Section III-B), and an information roadmap algorithm for escaping local minima (see Section III-C).

#### A. Information Potential Function

Because the number of targets correctly classified by a sensor cannot be established *a priori*, control objective (I) is achieved by maximizing the expected *information value* of the measurements, defined as the reduction of uncertainty in the target state  $X$  brought about by  $Z$ . The uncertainty of a discrete and random variable  $X$ , given another discrete and random variable  $Z$ , can be measured from its posterior PMF using the conditional Shannon entropy

$$H(X | Z) = - \sum_{x_i} \sum_{z_i} p_{X,Z}(x_i, z_i) \log_2 [p_{X|Z}(x_i | z_i)]. \quad (5)$$

Then, for three correlated random variables  $X$ ,  $Z$ , and  $E$ , the decrease in uncertainty of  $X$  due to  $Z$ , and given the value of  $E$ , can be measured by the conditional mutual information

$$\begin{aligned} I(X; Z | E) &= H(X | E) - H(X | Z, E) \\ &= \sum_{x_i} \sum_{z_i} \sum_{e_i} p_{X,Z,E}(x_i, z_i, e_i) \log_2 \left[ \frac{p_{X,Z|E}(x_i, z_i | e_i)}{p_{X|E}(x_i | e_i)p_{Z|E}(z_i | e_i)} \right]. \end{aligned} \quad (6)$$

Prior to obtaining a noisy measurement value  $z_i$ , the *expected* information value of target  $\mathcal{T}_i$  can be measured by the expected conditional mutual information

$$\begin{aligned} V_i &\triangleq \mathbb{E}_Z \{I(X; Z | e_i)\} = H(X | e_i) - \mathbb{E}_Z \{H(X | Z, e_i)\} \\ &= H(X) - \sum_{z_i} p_{Z|E}(z_i | e_i) H(X | z_i, e_i) \end{aligned} \quad (7)$$

where  $H(X | e_i) = H(X)$  because  $X$  and  $E$  are independent. The marginal PMF

$$p_{Z|E}(z_i | e_i) = \sum_x p_{Z|X,E}(z_i | x_i, e_i) p_X(x_i) \quad (8)$$

and all entropies in (7) can be computed from the PMFs in (2). If prior sensor measurements from the  $i$ th target are available, they can be treated similarly to  $e_i$  to obtain a nonmyopic measure of information value using (7), as shown in [6].

Then, the information value of a target can be mapped into the robotic sensor's configuration space through the following definition, taken from [6].

*Definition 3.1 (C-Target):* The target  $\mathcal{T}_i$  in  $\mathcal{W}$  maps in the robot's configuration space  $\mathcal{C}$  to the C-target region  $\mathcal{CT}_i = \{\mathbf{q} \in \mathcal{C} | \mathcal{S}(\mathbf{q}) \cap \mathcal{T}_i \neq \emptyset\}$ .

In the IP method, the information value and C-target region of every target in  $\mathcal{W}$  are used to construct an attractive potential

$$U_{\text{trg}}^i(\mathbf{q}) \triangleq \eta_1 \sigma V_i^b \left\{ 1 - \exp \left[ -\frac{\rho_i(\mathbf{q})^2}{2\sigma V_i^b} \right] \right\}, \quad i = 1, \dots, M \quad (9)$$

based on the minimum Euclidean distance between  $\mathbf{q}$  and  $\mathcal{T}_i$  in  $\mathcal{C}$ , i.e.,

$$\rho_i(\mathbf{q}) = \min_{\mathbf{q}' \in \mathcal{CT}_i} \|\mathbf{q}' - \mathbf{q}\|, \quad (10)$$

where  $\eta_1$  is a positive scaling factor that represents the importance of targets relative to other path-planning objectives,  $\|\cdot\|$  is the  $L_2$ -norm, and  $\sigma$  and  $b$  are two positive constants that determine the influence distance of the target. From (7), it can be seen that  $V_i$  is a constant up to the time when a new measurement is obtained from  $\mathcal{T}_i$ , for any  $i \in I_T$ , and that the attractive potential (9) is twice differentiable with respect to  $\mathbf{q}$ .

Then, the total attractive potential

$$U_{\text{att}}(\mathbf{q}) \triangleq \prod_{i=1}^M U_{\text{trg}}^i(\mathbf{q}) \quad (11)$$

can be shown to attain a local minimum at every C-target in  $\mathcal{C}$ , as follows. From (9) and (11), the gradient of the total attractive potential at  $\mathbf{q}$  is

$$\begin{aligned} & [\partial U_{\text{att}}(\mathbf{q})/\partial x \quad \partial U_{\text{att}}(\mathbf{q})/\partial y \quad \partial U_{\text{att}}(\mathbf{q})/\partial \theta] \\ & \triangleq \nabla U_{\text{att}}(\mathbf{q}) = \sum_{i=1}^M N_i(\mathbf{q}) \mathbf{n}_i(\mathbf{q}) \end{aligned} \quad (12)$$

where

$$N_i(\mathbf{q}) = \prod_{j \neq i} U_{\text{trg}}^j(\mathbf{q}) \eta_1 \rho_i(\mathbf{q}) \exp \left[ -\frac{\rho_i(\mathbf{q})^2}{2\sigma V_i^b} \right] \quad (13)$$

for  $i, j = 1, \dots, M$ , and  $\mathbf{n}_i \triangleq \nabla \rho_i$ . Thus, for any  $\mathbf{q}$ ,  $N_i$  represents a scaling factor for the local gradient  $\mathbf{n}_i$ , supported by a vector from  $\mathbf{q}$  to the closest point in  $\mathcal{CT}_i$ .

Two different repulsive potentials are defined for fixed and moving obstacles. Once detected, the mobility of the obstacle can be established using the Kalman filter and Stixel-world hybrid method developed in [39], which estimates an object's longitude, poses, and laterals from multiple camera images obtained over time. Then, for fixed obstacles, a potential barrier is generated around the C-obstacle region to prevent collisions, and, at the same time, to allow the robot to obtain measurements from targets nearby. For a fixed obstacle  $\mathcal{B}_l \subset \mathcal{W}$ , the C-obstacle  $\mathcal{CB}_l = \{\mathbf{q} \in \mathcal{C} \mid \mathcal{A}(\mathbf{q}) \cap \mathcal{B}_l \neq \emptyset\}$  is computed and used to determine the minimum distance from  $\mathbf{q}$  in configuration space, i.e.,

$$\varrho_l(\mathbf{q}) = \min_{\mathbf{q}' \in \mathcal{CB}_l} \|\mathbf{q} - \mathbf{q}'\|. \quad (14)$$

Let  $B$  denote the index set of fixed obstacles detected in  $\mathcal{W}$  up to the present time. Then, the repulsive potential for  $\mathcal{B}_l$ ,  $l \in B$ , is

$$U_{\text{obs}}^l(\mathbf{q}) \triangleq \begin{cases} \frac{1}{2} \eta_2 \left[ \frac{1}{\varrho_l(\mathbf{q})} - \frac{1}{d_0} \right]^2 U_{\text{att}}(\mathbf{q}), & \text{if } \varrho_l(\mathbf{q}) \leq d_0 \\ 0, & \text{if } \varrho_l(\mathbf{q}) > d_0 \end{cases} \quad (15)$$

where  $\eta_2$  is a positive scaling factor that represents the importance of fixed obstacles relative to other path-planning objectives, and  $d_0$  is the obstacle distance of influence [40]. By this novel definition of repulsive potential, a target within the distance of influence of an obstacle may be measured by the robotic sensor. In addition, as in classical PF, only obstacles that are within distance  $d_0$ , with index set  $B_0 = \{l \mid l \in B, \varrho_l(\mathbf{q}) \leq d_0\}$ , influence the robot motion.

Moving obstacles, such as other robots in  $\mathcal{W}$ , are assumed to have a configuration that is measured accurately in real time, but is not estimated at future time for lack of suitable models or computing power. Thus, the repulsive potential of a moving obstacle creates a virtual barrier in  $\mathcal{C}$ , regardless of the presence of targets within the distance of influence. Let  $R$  denote the index set of moving obstacles detected in  $\mathcal{W}$  up to the present time. Then, the repulsive potential for  $\mathcal{B}_j$  with  $j \in R$  is

$$U_{\text{rob}}^j(\mathbf{q}) \triangleq \begin{cases} \frac{1}{2} \eta_3 \left[ \frac{1}{\varrho_j(\mathbf{q})} - \frac{1}{d_0} \right]^2, & \text{if } \varrho_j(\mathbf{q}) \leq d_0 \\ 0, & \text{if } \varrho_j(\mathbf{q}) > d_0 \end{cases} \quad (16)$$

where  $\eta_3$  is a positive scaling factor that represents the importance of moving obstacles relative to other path-planning objectives. The index set  $R_0 = \{j \mid j \in R, \varrho_j(\mathbf{q}) \leq d_0\}$  contains the indices of all moving obstacles that are within the distance of influence from the robot contributing to the gradient of the potential function. Then, the total repulsive potential is defined as

$$U_{\text{rep}}(\mathbf{q}) \triangleq \sum_{l \in B_0} U_{\text{obs}}^l(\mathbf{q}) + \sum_{j \in R_0} U_{\text{rob}}^j(\mathbf{q}) \quad (17)$$

and the robotic sensor potential function is the sum of the attractive and repulsive potentials

$$U(\mathbf{q}) = U_{\text{att}}(\mathbf{q}) + U_{\text{rep}}(\mathbf{q}). \quad (18)$$

As in classical PF methods [40], the negative gradient of the potential function (18) represents a virtual force on the robotic sensor that is comprised of the sum of attractive and repulsive forces, generated by the corresponding potentials. In this paper, the attractive force is proportional to the information value of the target that generates it. The gradient of the potential function (18) can be obtained from (9)–(18) and simplified as follows

$$\begin{aligned} \nabla U(\mathbf{q}) &= \nabla U_{\text{att}}(\mathbf{q}) + \nabla U_{\text{rep}}(\mathbf{q}) = \sum_{l \in B_0} F_l(\mathbf{q}) \mathbf{v}_l(\mathbf{q}) \\ &+ \sum_{i=1}^M [N_i(\mathbf{q}) + A_i(\mathbf{q})] \mathbf{n}_i(\mathbf{q}) - \sum_{j \in R_0} \eta_3 \left[ \frac{1}{\varrho_j(\mathbf{q})} - \frac{1}{d_0} \right] \frac{\mathbf{v}_j(\mathbf{q})}{\varrho_j(\mathbf{q})^2} \end{aligned} \quad (19)$$

where

$$F_l(\mathbf{q}) \triangleq \eta_2 \left[ \frac{1}{\varrho_l(\mathbf{q})} - \frac{1}{d_0} \right] \frac{U_{\text{att}}(\mathbf{q})}{\varrho_l(\mathbf{q})^2} \quad (20)$$

and  $\mathbf{v}_l(\cdot) \triangleq \nabla \varrho_l(\cdot)$  is a vector supported by a vector between  $\mathbf{q}$  and the closest point in  $\mathcal{CB}_l$ , pointing away from  $\mathcal{CB}_l$ . The functions  $N_i(\cdot)$  have been defined in (13), while  $A_i(\cdot)$  is defined as follows:

$$\begin{aligned} A_i(\mathbf{q}) &\triangleq \frac{1}{2} \eta_1 \eta_2 \left\{ \sum_{l \in B_0} \left[ \frac{1}{\varrho_l(\mathbf{q})} - \frac{1}{d_0} \right]^2 \right\} \prod_{i \neq j} U_{\text{trg}}^j(\mathbf{q}) \rho_i(\mathbf{q}) \\ &\times \exp \left[ -\frac{\rho_i(\mathbf{q})^2}{2\sigma V_i^b} \right], \quad i = 1, \dots, M. \end{aligned} \quad (21)$$

In the next section, the gradient of the IP function (19) is used to develop a switched feedback control law for the robotic

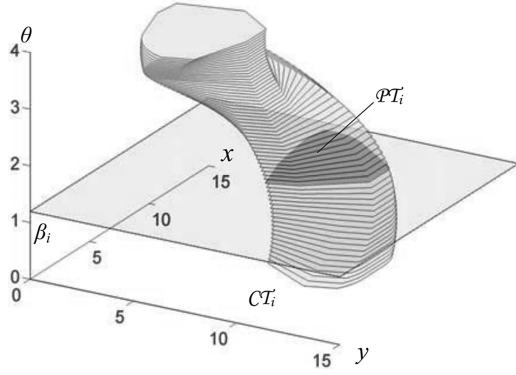


Fig. 2.  $\mathcal{PT}_i$  is the intersection of  $\mathcal{CT}_i$  with the horizontal plane  $\{x, y, \beta_i\}$ .

sensor that achieves the path planning and control objectives (I) and (II) and is asymptotically stable (see Section IV-B).

### B. Switched Control Law

In classical PF methods, the control law is obtained from a virtual force given by the negative gradient of the potential function. When this virtual force is used to control a nonholonomic robot, however, several issues arise including trapping in local minima, goals nonreachable with obstacles nearby, and stabilization. Other issues include oscillations and no passages between closely spaced obstacles. All of these issues are exacerbated by the presence of targets due to a higher density of local minima, and by the difficulty of reaching and stabilizing the robot in a C-target region in the presence of no-slip constraints. Besides compromising robot navigation, these issues can decrease the classification performance of the robotic sensor, especially when important targets are located near obstacles, local minima, or in narrow passages.

The control law is designed to switch from control inputs that are based only on the position vector  $\mathbf{x} \triangleq [x \ y]^T$ , to drive the robot near the target of highest information value, to control inputs that adjust the robot configuration  $\mathbf{q} = [\mathbf{x}^T \ \theta]^T$ , and to enable sensor measurements once the robot is near the target. This is accomplished by introducing a vector  $\mathbf{h}_i \in \mathcal{W}$  that points from  $\mathcal{O}_A$  to the target  $\mathcal{T}_i$ . Then, every vector

$$\mathbf{h}_i \triangleq \{\arg \min_{\mathbf{y} \in \mathcal{CT}_i} \|\mathbf{y} - \mathbf{x}\| - \mathbf{x}\}, \quad i \in I_T \quad (22)$$

specifies a goal orientation  $\beta_i$  defined as the angle that the projection of  $\mathbf{h}_i$  onto the inertial  $xy$ -plane makes with the  $x$ -axis. Let  $\mathcal{PT}_i$  denote the intersection of  $\mathcal{CT}_i$  with the horizontal plane  $\{x, y, \beta_i\}$ , as shown in Fig. 2. Under the assumptions in Section II,  $\mathcal{PT}_i$  is a polygon for which it is possible to define and compute an inscribed circle (see Fig. 3) defined as the largest circle that is contained by the closure of  $\mathcal{PT}_i$ .

Now, let  $\xi_i$  and  $r_i$  denote the center and radius of the inscribed circle in  $\mathcal{PT}_i$ , respectively, and  $\epsilon \in (0, r_i)$  denote a positive constant chosen by the user. As illustrated in Fig. 4, the goal of the switched control law is to bring the robot configuration within a distance  $\epsilon$  of a 3-D line segment in  $\mathcal{C}$ , defined as the set  $\lambda_i = \{(x, y, \theta) : [x \ y]^T = \xi_i, 0 \leq \theta \leq 2\pi\}$ . Subse-

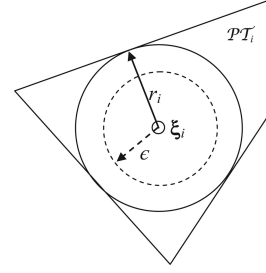


Fig. 3. Inscribed circle for polygon  $\mathcal{PT}_i$  with center  $\xi_i$  and radius  $r_i$ .

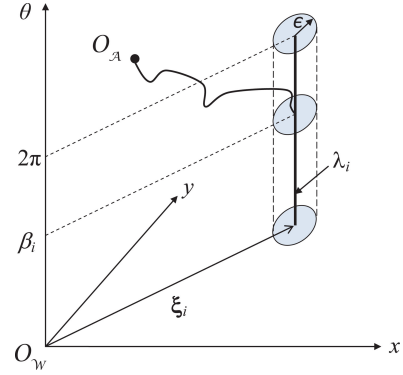


Fig. 4. Goal of switched control law for an inscribed circle with center  $\xi_i$ , and a positive constant  $\epsilon$ .

quently, the control law is switched to adjust the robot orientation to meet  $\beta_i$  by means of the vector

$$\mathbf{h} \triangleq \arg \min \{\|\mathbf{h}_i\|, i \in I_T\} \quad (23)$$

such that, when  $\|\mathbf{h}\| > \epsilon$ , the potential function  $U$  is defined in terms of the distance

$$\rho_i(\mathbf{q}) = \|\xi_i - \mathbf{x}\| \quad (24)$$

to bring  $\mathbf{q}$  within an  $\epsilon$  of  $\lambda_i$ . Then, the potential-based control law is given by

$$u_1 = a = -\mathbf{S}(\mathbf{q})^T \nabla U(\mathbf{q}) - k_1 v \quad (25)$$

where  $\mathbf{S}(\mathbf{q}) \triangleq [\cos \theta \ \sin \theta \ 0]^T$ ,  $k_1$  is a positive constant, and

$$u_2 = w = \dot{\alpha}[U(\mathbf{q})] + k_0 \{\alpha[U(\mathbf{q})] - \theta\} \quad (26)$$

where  $\alpha$  is the orientation angle of vector  $\partial_x U \triangleq [\partial_x U(\mathbf{q}) \ \partial_y U(\mathbf{q})]^T$  in the inertial  $xy$ -plane, and  $k_0$  is a positive constant.

The orientation angle,  $\alpha$ , and its time derivative can be obtained from the components of (19) as follows:

$$\alpha[U(\mathbf{q})] = 2 \arctan \left[ \frac{\frac{\partial U(\mathbf{q})}{\partial y}}{\sqrt{\left(\frac{\partial U(\mathbf{q})}{\partial y}\right)^2 + \left(\frac{\partial U(\mathbf{q})}{\partial x}\right)^2}} + \frac{\partial U(\mathbf{q})}{\partial x} \right] + \pi \quad (27)$$

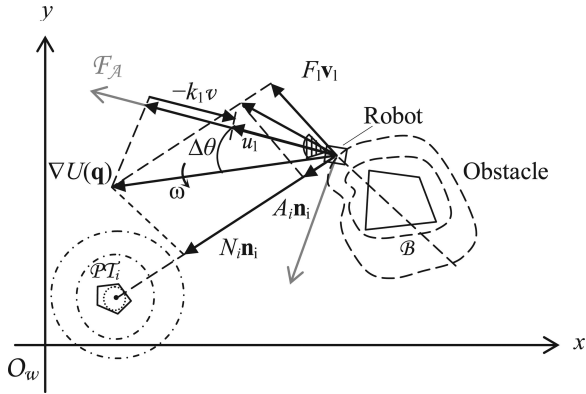


Fig. 5. Construction of switched control law based on the components of the potential function gradient  $\nabla U(\mathbf{q})$ , for  $\|\mathbf{h}_i\| > \epsilon$ .

$$\begin{aligned} \dot{\alpha}[U(\mathbf{q})] = & \frac{\frac{\partial U(\mathbf{q})}{\partial x}}{\left(\frac{\partial U(\mathbf{q})}{\partial x}\right)^2 + \left(\frac{\partial U(\mathbf{q})}{\partial y}\right)^2} \left[ \frac{\partial^2 U(\mathbf{q})}{\partial x \partial y} \dot{x} + \frac{\partial^2 U(\mathbf{q})}{\partial y^2} \dot{y} \right] \\ & - \frac{\frac{\partial U(\mathbf{q})}{\partial y}}{\left(\frac{\partial U(\mathbf{q})}{\partial x}\right)^2 + \left(\frac{\partial U(\mathbf{q})}{\partial y}\right)^2} \left[ \frac{\partial^2 U(\mathbf{q})}{\partial x \partial y} \dot{y} + \frac{\partial^2 U(\mathbf{q})}{\partial x^2} \dot{x} \right]. \end{aligned} \quad (28)$$

The role of each gradient component in the construction of (25) is schematized in Fig. 5.

When  $\|\mathbf{h}\| \leq \epsilon$ , the distance in (10) is computed with respect to the geometric dilatation of the C-target,  $\mathcal{CT}'_i \triangleq \{\mathbf{q} \in \mathbb{R}^3 \mid \mathbf{x} = \delta_r(\mathbf{x}' - \boldsymbol{\xi}_i) + \boldsymbol{\xi}_i, \forall \mathbf{x}' \in \mathcal{PT}_i, 0 \leq \theta \leq 2\pi\}$ , where

$$\delta_r = \frac{(r_i - C)}{\max_{\mathbf{x} \in \mathcal{PT}_i} \|\mathbf{h}_i\|} \quad (29)$$

is the scale factor, and  $C \in (0, r_i)$  is a constant chosen by the user. Then, for  $\|\mathbf{h}\| \leq \epsilon$ , the potential-based control law is switched to

$$u_1 = a = -k_p \mathbf{S}(\mathbf{q})^T \nabla U(\mathbf{q}) - k_1 v \quad (30)$$

where  $k_1$  and  $k_p$  are positive constants, and

$$u_2 = w = k_0(\beta_i - \theta). \quad (31)$$

Because  $\mathcal{PT}_i$  is a polygonal curve, the geometric dilatation  $\mathcal{CT}'_i$  can be computed efficiently, as shown in [41]. The positive constants  $C$  and  $\epsilon$  are chosen based on the units and dimensions of the C-targets to ensure that they each lie in the interval  $(0, r_i)$ , for any  $i \in I_T$ . The constant  $k_p$  is chosen by the user to satisfy the inequality

$$k_p > (v_{\max}^2 + 4\pi^2)/[2(\vartheta - \varphi)] \quad (32)$$

where  $\vartheta$  is a positive constant that bounds the potential function  $U$  from below when  $\rho_i = r_i$ , and  $\varphi$  is another positive constant that bounds  $U$  from above when  $\rho_i = \epsilon$ . Then, the movement of the robotic sensor is constrained into the cylinder shown in Fig. 4, within which  $\|\boldsymbol{\xi}_i - \mathbf{x}\| < r_i$ , and, thus, the sensor is guaranteed to obtain measurements from target  $\mathcal{T}_i$ , i.e.,  $\mathcal{T}_i \cap \mathcal{S}(\mathbf{q}) \neq \emptyset$ . Constants  $k_0$  and  $k_1$  are chosen based on the desired convergence rate and maximum overshoot. As shown in Section IV-B, by this approach, the control law is asymptotically stable and guarantees that sensor measurements can be obtained

from a target  $\mathcal{T}_i$ . Furthermore, to account for the discontinuity of the control signal, the IIR filter

$$\begin{bmatrix} u_1^*(t) \\ u_2^*(t) \end{bmatrix} = e^{-\frac{T_s}{\tau}} \begin{bmatrix} u_1^*(t - T_s) \\ u_2^*(t - T_s) \end{bmatrix} + \left(1 - e^{-\frac{T_s}{\tau}}\right) \begin{bmatrix} u_1(t) \\ u_2(t) \end{bmatrix} \quad (33)$$

can be inserted between the switched control law and the robot [42]. Here,  $\tau$  is the time constant and the sampling period  $T_s$  is 0.01 (s). The simulations show that increasing the value of  $\tau$  results in shorter distance traveled but higher control usage, and that the highest overall efficiency (as defined in Section V) is obtained for  $\tau > 0.02$  (s).

### C. Information Roadmap for Escaping Local Minima

A well-known limitation of PF methods is that the robot can be trapped in local minima of  $U$  and not reach its goal configuration [40]. When there exist multiple targets in  $\mathcal{W}$ , the number of local minima typically increases, and, since the robotic sensor is attracted to the targets, trapping can impair its ability to obtain target measurements. This section presents a new method for escaping local minima while increasing the probability of obtaining sensor measurements, subject to the robot kinematics (1). The method is based on the observation that the IP function defined in (18) can be utilized to derive a probability density function (PDF) for sampling milestones and building a local roadmap representation of the free configuration space. Unlike traditional sampling methods for path planning [43], the method presented in this section takes into account the robot kinematics (1) to verify connectivity between milestones. As a result, after escaping a local minimum, the robotic sensor configuration can be proven to asymptotically converge to the milestone with the lowest potential (or highest information value).

A milestone  $\mathbf{m}_l$  is defined as any possible value of the robot configuration  $\mathbf{q} \in \mathcal{C}$ , which, during sampling, is viewed as a continuous random vector. The PDF of a 3-D continuous random vector is a joint PDF of the three elements, given by a nonnegative function  $f_{\mathbf{q}}$ , such that

$$\mathbf{P}(\mathbf{q} \in Q) = \int_Q f_{\mathbf{q}}(\mathbf{q}) d\mathbf{q} = \int \int \int_Q f_{\mathbf{q}}(x, y, \theta) dx dy d\theta \quad (34)$$

for any subspace  $Q \subset \mathcal{C}$ . To qualify as a PDF,  $f_{\mathbf{q}}$  must also obey the normalization property

$$\int_{-\infty}^{\infty} f_{\mathbf{q}}(\mathbf{q}) d\mathbf{q} = 1. \quad (35)$$

Suppose the robotic sensor arrives at a local minimum  $\mathbf{m}_0$  of  $U$ . Then, a PDF that obeys the above properties is obtained over a randomly generated subspace  $Q \subset \mathcal{C}$ , such that  $\mathbf{m}_0 \in Q$ , by letting

$$f_{\mathbf{q}}(\mathbf{q}) = \begin{cases} \frac{\exp[-U(\mathbf{q})]}{\int_Q \exp[-U(\mathbf{q})] d\mathbf{q}}, & \mathbf{q} \in Q \\ 0, & \mathbf{q} \notin Q. \end{cases} \quad (36)$$

From (36), it can be seen that the probability of a sample falling in a region of  $Q$  is higher (lower) where the value of  $U$  is lower (higher). As a result, configurations in  $Q$  that are close to or

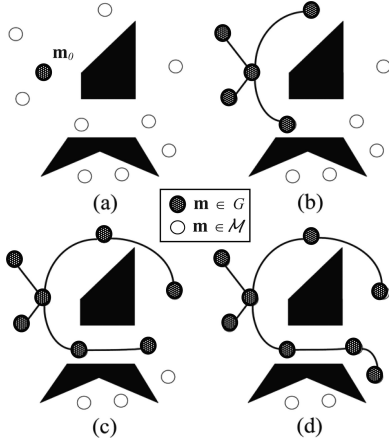


Fig. 6. Process to construct the roadmap. (a) Initial milestones. (b) First step. (c) Second step. (d) Final step. Local minima (dash circle); Milestones (white circle); C-obstacles (black area).

inside C-targets with high information value, and that are far away from obstacles, are sampled with higher probability.

Using a direct method [44],  $\kappa$  milestones are sampled from (36), and used to construct an ordered set  $\mathcal{M} = \{\mathbf{m}_0, \dots, \mathbf{m}_\kappa\}$ . A local roadmap is then constructed by building an undirected graph  $G = \{(\mathbf{m}_l, \mathbf{m}_i) : \mathbf{m}_l, \mathbf{m}_i \in \mathcal{M}, l \neq i\}$ , starting with the local minimum  $\mathbf{m}_0 \in Q$ , and using a local planner to connect  $\mathbf{m}_0$  to other milestones in  $\mathcal{M}$ , until no reachable milestones are left in  $\mathcal{M}$ . As schematized in Fig. 6, the local planner connects any two milestones  $\mathbf{m}_l, \mathbf{m}_i \in \mathcal{M}$ , with  $i > l$ , provided that there exist control inputs (25) and (26) that can bring  $\mathbf{q}$  from  $\mathbf{m}_l$  to  $\mathbf{m}_i$  in a finite time interval  $[t_l, t_i]$  subject to (1), and with  $(t_i - t_l) < t_f$ , where  $t_f$  is a predefined time limit chosen by the user, and  $[\xi_i^T \beta_i]^T = \mathbf{m}_i$ .

Assume that the path connecting  $\mathbf{m}_l$  to  $\mathbf{m}_i$  can be parameterized by a vector function  $\gamma_i : t \rightarrow \mathbf{q}$ , where  $t \in [t_l, t_i]$ . Then, the algorithm connects  $\mathbf{m}_l$  to  $\mathbf{m}_i$ , if there exists a time  $t^* \in (t_l, t_i)$  such that

$$\|\gamma_i(t^*) - \mathbf{m}_i\| \leq \varepsilon \quad (37)$$

where  $\varepsilon$  is a positive constant, and for any  $t \in [t_l, t^*] \subset [t_l, t_i]$

$$\|\gamma_i(t) - \mathbf{m}_i\| > \varepsilon. \quad (38)$$

As illustrated in Fig. 6, at every step of the algorithm, all the milestones in  $\mathcal{M}$  that can be connected to a milestone already in  $G$  are added to  $G$ , and deleted from  $\mathcal{M}$  [see Fig. 6(b) and (c)]. The algorithm continues until there are no more milestone in  $\mathcal{M}$  and then milestones that remain unconnected [see Fig. 6(d)] are discarded. As shown in the next section, after building the roadmap  $G$ , an escape path leading to a target can be obtained in a finite number of iterations. In addition, through this path, the robotic sensor has a higher probability to converge to a target with higher information value.

#### IV. ANALYSIS OF INFORMATION POTENTIAL METHOD

This section analyzes the properties of the IP method presented in the previous section. In particular, it is shown that the IP presented in Section III-A satisfies the properties of potential navigation functions [45]; the switched control law presented in

Section III-B is asymptotically stable; the information roadmap method presented in Section III-C is guaranteed to find an escape path to a C-target using a finite number of iterations; the target of highest information value has the highest probability of being measured by the robotic sensor; and the average computational complexity of the escape algorithm is less than  $O(n^2)$ .

##### A. Properties of Attractive Potential

The IP  $U_{\text{trg}}^i$ , defined in (9), obeys the following properties.

- 1)  $U_{\text{trg}}^i$  is an increasing function of  $\rho_i$ , defined in (10) as the distance between the robot and the target  $\mathcal{T}_i$ .

*Proof:* From (9), the first-order derivative of the IP of  $\mathcal{T}_i$  with respect to  $\rho_i$  is a nonnegative exponential function

$$\frac{\partial U_{\text{trg}}^i(\rho_i)}{\partial \rho_i} \triangleq g(\rho_i) = \eta_1 \rho_i \exp \left[ -\frac{\rho_i^2}{2\sigma V_i^b} \right] \quad (39)$$

where  $\rho_i \geq 0$  and  $\eta_1$ ,  $\sigma$ , and  $b$  are positive constants. It follows that  $U_{\text{trg}}^i$  is an increasing function of  $\rho_i$ . ■

- 2) As  $\rho_i \rightarrow \infty$ ,  $U_{\text{trg}}^i$  converges to a finite positive value.

*Proof:* From (9)

$$\lim_{\rho_i \rightarrow \infty} U_{\text{trg}}^i(\rho_i) = \eta_1 \sigma V_i^b \quad (40)$$

where  $V_i$  is the information value defined in (7). For any two dependent random variables  $X$  and  $Z$ ,  $I(X; Z | e_i) > 0$ , for all  $e_i$  [47, p. 27]. Similarly,  $V_i = \mathbb{E}_Z \{I(X; Z | e_i)\} > 0$ , because  $\mathbb{E}_Z \{H(X; Z | e_i)\} \geq H(X | e_i)$  for all  $e_i$ . Furthermore, from the properties of entropy,  $H(\cdot) \leq 1$ . Thus, it can be easily shown that, since  $b > 0$ ,  $0 < V_i^b \leq 1$ . It follows that the limit in (40) is a finite positive value. ■

- 3) Let  $d_i$  denote the distance of influence of  $\mathcal{T}_i$ . Then, for any  $i, j \in I_T$ , if  $V_i > V_j$ , it follows that  $d_i > d_j$ .

*Proof:* From (39), the second-order derivative

$$\frac{\partial^2 U_{\text{trg}}^i(\rho_i)}{\partial \rho_i^2} = \frac{\partial g(\rho_i)}{\partial \rho_i} = \eta_1 \left[ 1 - \frac{\rho_i^2}{\sigma V_i^b} \right] \exp \left[ -\frac{\rho_i^2}{2\sigma V_i^b} \right] \quad (41)$$

is a monotonically decreasing function of  $\rho_i$ . Because the distance of influence is the inflection point  $\rho_i^*$  of  $U_{\text{trg}}^i$ , at which  $g(\rho_i^*) = g'(\rho_i^*) = 0$ , it follows that  $d_i = \rho_i^* = \sqrt{\sigma V_i^b}$ . Then, since  $\sigma, b > 0$ ,  $d_i$  is an increasing function of  $V_i$ . ■

##### B. Closed-Loop Stability of Switched Feedback Control Law

The switched control law presented in Section III-B can be proven to be asymptotically stable under the following simplifying assumptions: (I)  $\mathbf{q}$  is within the influence distance of only one target  $\mathcal{T}_i$ , such that  $\rho_i(\mathbf{q}) < d_i$ , and  $\rho_j(\mathbf{q}) > d_j$  for all  $j \in I_T$ ,  $j \neq i$ ; and (II) there are no obstacles within a distance  $d_0$ , i.e.,  $B_0 = R_0 = \emptyset$ . Assumptions (I) and (II) can be satisfied by choosing proper values of the parameters  $\sigma$ ,  $b$ , and  $d_0$ .

*Proof:* Under assumptions (I) and (II), the gradient of the potential function (19) is

$$\nabla U(\mathbf{q}) = N_i \mathbf{n}_i(\mathbf{q}) = \eta_1 \rho_i(\mathbf{q}) \exp \left[ -\frac{\rho_i(\mathbf{q})^2}{2\sigma V_i^b} \right] \nabla \rho_i \quad (42)$$

and the gradient of  $\rho_i$  in  $\mathcal{F}_W$  is

$$\nabla \rho_i = \left[ \frac{1}{\rho_i(\mathbf{q})} (\boldsymbol{\xi}_i - \mathbf{x}) \quad 0 \right]^T. \quad (43)$$

From (42) and (43), the gradient of the potential function can be rewritten as

$$\nabla U(\mathbf{q}) = [K(\boldsymbol{\xi}_i - \mathbf{x}) \quad 0]^T \quad (44)$$

where  $K \triangleq \eta_1 \exp[-\rho_i(\mathbf{q})^2 / (2\sigma V_i^b)]$ .

Now, consider the Lyapunov function candidate

$$\mathcal{V}(\boldsymbol{\chi}) = U(\mathbf{q}) + \frac{1}{2}v^2 + \frac{1}{2}\{\alpha[U(\mathbf{q})] - \theta\}^2 \quad (45)$$

where  $\alpha[\cdot]$  is the orientation angle introduced in (26). Since  $U(\mathbf{q}) > 0$ , and the term  $v^2 + \{\alpha[U(\mathbf{q})] - \theta\}^2 \geq 0$ , it follows that  $\mathcal{V}(\boldsymbol{\chi}) > 0$  for all  $\boldsymbol{\chi} \in \mathbb{R}^4$ . From the unicycle kinematics (1) and the control law (25) and (26), the time derivative of  $\mathcal{V}$  for the *closed-loop* system is

$$\begin{aligned} \dot{\mathcal{V}}(\boldsymbol{\chi}) &= \nabla U(\mathbf{q})^T \dot{\mathbf{q}} + v\dot{v} + \{\alpha[U(\mathbf{q})] - \theta\} \{\dot{\alpha}[U(\mathbf{q})] - \dot{\theta}\} \\ &= \nabla U(\mathbf{q})^T \begin{bmatrix} \cos \theta & 0 \\ \sin \theta & 0 \\ 0 & 1 \end{bmatrix} \begin{bmatrix} v \\ w \end{bmatrix} \\ &\quad + v [-\mathbf{S}(\mathbf{q})^T \nabla U(\mathbf{q}) - k_1 v] - k_0 \{\alpha[U(\mathbf{q})] - \theta\}^2 \\ &= \nabla U(\mathbf{q})^T \mathbf{S}(\mathbf{q})v \\ &\quad - \mathbf{S}(\mathbf{q})^T \nabla U(\mathbf{q})v - k_1 v^2 - k_0 \{\alpha[U(\mathbf{q})] - \theta\}^2 \\ &= -k_1 v^2 - k_0 \{\alpha[U(\mathbf{q})] - \theta\}^2 \leq 0. \end{aligned} \quad (46)$$

Since  $\mathcal{V}(\boldsymbol{\chi})$  is radially unbounded, given any positive constant  $c$ , the set  $\Omega_c = \{\boldsymbol{\chi} \in \mathbb{R}^4 \mid \mathcal{V}(\boldsymbol{\chi}) \leq c\}$  is a compact positively invariant set. For the robotic sensor, the value of  $c$ , and thus the region of attraction, can be determined based on the bound in (40) and the maximum linear velocity  $v_{\max}$ . We want to show that every trajectory starting in  $\Omega_c$  approaches the equilibrium set  $\mathcal{E} = \{\boldsymbol{\chi} \in \mathbb{R}^4 \mid \boldsymbol{\chi} = [\boldsymbol{\xi}_i^T \alpha[U(\boldsymbol{\xi}_i)] 0]^T\}$  as  $t \rightarrow \infty$ .

The set  $\Upsilon$  of all points in  $\Omega_c$  where  $\dot{\mathcal{V}}(\boldsymbol{\chi}) = 0$  is  $\Upsilon = \{\boldsymbol{\chi} \in \Omega_c \mid \theta = \alpha[U(\mathbf{q})], v = 0\}$ . Then, it can be shown that  $\mathcal{E}$  is the largest invariant set in  $\Upsilon$  because for any  $\boldsymbol{\chi} \in \{\Upsilon \setminus \mathcal{E}\}$

$$\begin{aligned} \dot{v} &= u_1 = -\mathbf{S}(\mathbf{q})^T \nabla U(\mathbf{q}) - k_1 v \\ &= [\cos\{\alpha[U(\mathbf{q})\} \sin\{\alpha[U(\mathbf{q})\} 0] \nabla U(\mathbf{q}) \\ &= \frac{\nabla U(\mathbf{q})^T}{|\nabla U(\mathbf{q})|} \nabla U(\mathbf{q}) = |\nabla U(\mathbf{q})| \neq 0 \end{aligned} \quad (47)$$

where  $\{\Upsilon \setminus \mathcal{E}\}$  denotes the complement set of  $\mathcal{E}$  in  $\Upsilon$ . Thus, any trajectory starting in  $\{\Upsilon \setminus \mathcal{E}\}$  cannot stay identically in  $\Upsilon$ . On the other hand, any trajectory starting at a point in  $\mathcal{E}$  will remain identically in  $\Upsilon$ , because  $\dot{\boldsymbol{\chi}} = 0$ . Since  $\mathcal{E}$  is the largest invariant set in  $\Upsilon$ , it follows from LaSalle's invariance principle [48, p. 128] that every trajectory starting in  $\Omega_c$  approaches  $\mathcal{E}$  as  $t \rightarrow \infty$ .

When  $\|\mathbf{h}\| \leq \epsilon$ , consider the candidate Lyapunov function

$$\mathcal{V}(\boldsymbol{\chi}) = k_p U(\mathbf{q}) + \frac{1}{2}v^2 + \frac{1}{2}(\beta_i - \theta)^2. \quad (48)$$

From the unicycle model (1) and the control law (30) and (31), the time derivative of  $\mathcal{V}$  for the *closed-loop* system can be written

as

$$\dot{\mathcal{V}}(\boldsymbol{\chi}) = -k_1 v^2 - k_0 (\beta_i - \theta)^2 \leq 0. \quad (49)$$

Since  $\epsilon < r_i$ , any time  $\|\mathbf{h}\| \leq \epsilon$ , the state of the closed-loop system is a point in the set  $\Omega_r = \{\boldsymbol{\chi} \in \mathbb{R}^4 \mid \|\mathbf{h}\| \leq r_i, 0 \leq \theta \leq 2\pi, \|v\| < v_{\max}\}$ . Let  $\phi = \min_{\|\mathbf{h}\|=r_i} \mathcal{V}(\boldsymbol{\chi})$  in  $\Omega_r$ , where from Section IV-A it can be easily shown that  $\phi > 0$ . Take  $c \in (0, \phi)$  and let  $\Omega_c = \{\boldsymbol{\chi} \in \Omega_r \mid \mathcal{V}(\boldsymbol{\chi}) \leq c\}$ . We want to show that every trajectory starting in  $\Omega_c$  approaches the equilibrium set  $\mathcal{E} = \{\boldsymbol{\chi} \in \Omega_c \mid [\cos \beta_i \sin \beta_i] \partial_{\mathbf{x}} U = 0, \theta = \beta_i, v = 0\}$  as  $t \rightarrow \infty$ .

The set  $\Upsilon$  of all points in  $\Omega_c$  where  $\dot{\mathcal{V}}(\boldsymbol{\chi}) = 0$  is  $\Upsilon = \{\boldsymbol{\chi} \in \Omega_c \mid \theta = \beta_i, v = 0\}$ . Then, it can be shown that  $\mathcal{E}$  is the largest invariant set in  $\Upsilon$  because for any  $\boldsymbol{\chi} \in \{\Upsilon \setminus \mathcal{E}\}$

$$\begin{aligned} \dot{v} &= u_1 = -k_p \mathbf{S}(\mathbf{q})^T \nabla U(\mathbf{q}) - k_1 v \\ &= -k_p [\cos \beta_i \sin \beta_i 0] \nabla U(\mathbf{q}) \\ &= -k_p [\cos \beta_i \sin \beta_i] \partial_{\mathbf{x}} U \neq 0 \end{aligned} \quad (50)$$

by definition of  $\mathcal{E}$ . Thus,  $\mathcal{E}$  is the largest invariant set in  $\Upsilon$ , because any trajectory starting in  $\{\Upsilon \setminus \mathcal{E}\}$  cannot remain identically in  $\Upsilon$ . On the other hand, any trajectory starting at a point in  $\mathcal{E}$  will remain identically in  $\Upsilon$ , because  $\dot{\boldsymbol{\chi}} = 0$ . It follows from LaSalle's invariance principle [48, p. 128] that every trajectory starting in  $\Omega_c$  approaches  $\mathcal{E}$  as  $t \rightarrow \infty$ . ■

### C. Expected Number of Iterations of Information Roadmap Algorithm

The potential-based switched control law presented in Section III-B may cause the robot to be trapped in a local minimum of the potential function (18), defined as a stationary point of  $U$  with a positive definite Hessian matrix  $\partial^2 U / \partial \mathbf{q}^2 > 0$  and zero information value. In this case, it can be shown that the roadmap  $G$  containing an escape path leading to a C-target can be obtained in a finite number of iterations. Assume there exist a finite number of local minima in  $U$  and all the configurations in  $Q \subset \mathcal{C}$  are reachable under the switched control law (25)–(31). In addition, assume the subspace  $Q \subset \mathcal{C}$  (defined in Section III-C) contains at least one C-target. Then,  $Q$  can be partitioned into  $(m+n)$  compact subspaces  $g_1, \dots, g_m$  and  $h_1, \dots, h_n$ , such that for any  $\mathbf{q} \in g_j \subset Q$ , the robot will converge to a configuration  $\mathbf{q} \in \mathcal{CT}_j \subset Q$ , and for any  $\mathbf{q} \in h_l \subset Q$ , the robot will converge to a local minimum  $\tilde{\mathbf{q}}_l \in Q$ . Now, for a robot trapped at  $\tilde{\mathbf{q}}_i$  the probability of sampling a milestone  $\mathbf{m}$  in  $g_j$  is

$$\mathbf{P}(\{\mathbf{m} \in g_j\} \mid \{\mathbf{q} = \tilde{\mathbf{q}}_i\}) = \int_{\mathbf{q}' \in g_j} f_{\mathbf{q}}(\mathbf{q}') d\mathbf{q}' \triangleq p(h_i, g_j) \quad (51)$$

and the probability of sampling a milestone  $\mathbf{m}$  in  $h_i$  is

$$\mathbf{P}(\{\mathbf{m} \in h_i\} \mid \{\mathbf{q} = \tilde{\mathbf{q}}_i\}) = \int_{\mathbf{q}' \in h_i} f_{\mathbf{q}}(\mathbf{q}') d\mathbf{q}' \triangleq p(h_i, h_i) \quad (52)$$

where  $f_{\mathbf{q}}(\cdot)$  is the PDF defined in (36).

Since all milestones in  $G$  are reachable they are connected, and  $p(h_i, g_j)$  denotes the probability that the robot will converge from  $\tilde{\mathbf{q}}_i$  to  $\mathcal{CT}_j$ , while  $p(h_i, h_l)$  denotes the probability that it will converge from  $\tilde{\mathbf{q}}_i$  to another local minimum  $\tilde{\mathbf{q}}_l$ .

Furthermore, since the probabilities in (51) and (52) are independent of the robot position, its movement can be modeled as a Markov chain, as shown in [48]. In particular, for a robot controlled by the IP method, the transition matrix, denoted by  $\mathbf{M}$ , can be written in terms of the probabilities in (51) and (52), as shown in (68). In addition, (68) can be partitioned as follows

$$\mathbf{M} = \begin{bmatrix} \mathbf{I}_m & \mathbf{R} \\ \mathbf{A} & \mathbf{B} \end{bmatrix} \quad (53)$$

where  $\mathbf{I}_m$  is an  $m \times m$  identity matrix. Under the stated assumptions,  $\mathbf{R} \in \mathbb{R}^{m \times n}$  is a zero matrix, because when  $\tilde{\mathbf{q}}_i \in g_j$  no sampling is necessary.  $\mathbf{A} \in \mathbb{R}^{n \times m}$  and  $\mathbf{B} \in \mathbb{R}^{n \times n}$  are matrices with nonnegative entries because  $f_{\mathbf{q}}(\cdot)$  is a nonnegative function.

By the properties of probability functions, the sum of the entries in every row of  $\mathbf{B}$  is less than one, i.e., every element of the vector  $\mathbf{B}\mathbf{n}$  is less than one, where  $\mathbf{n} \triangleq \mathbf{1}_{n \times 1}$ . From Gershgorin's theorem [49], it follows that all eigenvalues of  $\mathbf{B}$  are less than one [50], and  $\lim_{\ell \rightarrow \infty} \mathbf{B}^\ell \rightarrow 0$ , where  $\mathbf{B}^\ell$  represents the matrix  $\mathbf{B}$  raised to the  $\ell$  power. It also follows that the matrix inverse  $(\mathbf{I}_n - \mathbf{B})^{-1} \triangleq \mathbf{C}$  exists and can be written as

$$\mathbf{C} = \mathbf{CB} + \mathbf{I}_n. \quad (54)$$

It can be shown using the approach in [51] that the expected number of times that the Markov chain will visit  $h_k$  prior to  $g_j$ , when starting at  $h_i$ , is equal to  $\mathbf{C}_{(i,k)}$ . Then, from (68) and  $\mathbf{C}_{(i,k)} \geq 0$ , whenever sampling starts at the event  $\{\mathbf{q} = \tilde{\mathbf{q}}_i\}$ , the sampling event  $\{\mathbf{m} \in h_i\}$  is expected to take place  $c_i$  times prior to event  $\{\mathbf{m} \in g_j\}$ , where

$$c_i \triangleq \sum_{k=1}^n \mathbf{C}_{(i,k)}. \quad (55)$$

Multiplying (54) by  $\mathbf{n}$ , and letting  $\mathbf{c} \triangleq [c_1 \cdots c_n]^T$ , it follows that

$$\mathbf{C}\mathbf{n} = \mathbf{CB}\mathbf{n} + \mathbf{I}_n\mathbf{n} = \mathbf{CB}\mathbf{n} + \mathbf{n} = \mathbf{c} \quad (56)$$

and

$$\mathbf{c} \leq \gamma \mathbf{C}\mathbf{n} + \mathbf{n} = \gamma \mathbf{c} + \mathbf{n} \quad (57)$$

where  $\gamma$  denotes the largest element in  $\mathbf{B}\mathbf{n}$ . For two matrices  $\mathbf{A}$  and  $\mathbf{B}$  with the same dimensions, the inequality  $\mathbf{A} \leq \mathbf{B}$  means that  $\mathbf{A}_{(i,j)} \leq \mathbf{B}_{(i,j)}$ , for all  $(i,j)$ . Thus, from (57), the expected number of iterations  $c_i$  is finite for all  $i$  and has the upper bound (UB)  $1/(1 - \gamma)$ .

### D. Properties of Information Roadmap Method

The information roadmap method presented in Section III-C is designed not only to help the robotic sensor escape local minima, but also to increase the probability of obtaining valuable sensor measurements in the process. In particular, it can be shown that given two targets  $\mathcal{T}_j$  and  $\mathcal{T}_\ell$ , with the same geometry but different information value, say  $V_j > V_\ell$ , the robot configuration has a higher probability of converging to  $\mathcal{CT}_j$  than to  $\mathcal{CT}_\ell$ , assuming the two paths from  $\tilde{\mathbf{q}}_i$  to the targets are otherwise equivalent. Hence, targets with higher information value have

a higher probability of being measured by the robotic sensor when it escapes a local minimum  $\tilde{\mathbf{q}}_i$ .

Since the targets have the same geometry, it can be assumed without loss of generality that subspaces  $g_j$  and  $g_\ell$  have the same geometry. For example,  $g_j$  and  $g_\ell$  could be disks of radii  $d_j$  and  $d_\ell$ , respectively. From (68), the probability that the robotic sensor will move from a milestone in  $g_j$  to a milestone in  $h_i$  is

$$P_G(h_i, g_j) = \sum_{k=1}^n p(h_i, h_k) P_G(h_k, g_j) + p(h_i, g_j) \quad (58)$$

or, in matrix notation

$$\mathbf{H} = \mathbf{BH} + \mathbf{A} \quad (59)$$

where  $\mathbf{H}_{(i,j)} = P_G(h_i, g_j)$ . From Section IV-C, the matrix  $(\mathbf{I}_n - \mathbf{B})$  is nonsingular; therefore, (59) can be written as

$$\mathbf{H} = (\mathbf{I}_n - \mathbf{B})^{-1} \mathbf{A} = \mathbf{CA}. \quad (60)$$

Since the paths to the two targets are assumed equivalent, they can be represented by the same transition probabilities, and  $\mathbf{C}$  has the same value for both targets.

Now, recall from (36) that the PDF  $f_{\mathbf{q}}(\mathbf{q})$  is an increasing function of the information value (6) associated with  $\mathbf{q}$ . In addition, the information value for all  $\mathbf{q} \in \mathcal{CT}_j$  is  $V_j$ , and the information value for all  $\mathbf{q} \in \mathcal{CT}_\ell$  is  $V_\ell$ . Since  $g_j$  and  $g_\ell$  have the same geometry, and map into C-targets  $\mathcal{CT}_j$  and  $\mathcal{CT}_\ell$ , it follows from (51) that  $p(h_k, g_j) > p(h_k, g_\ell)$  for any  $h_k \in Q$ , and from (60)

$$\begin{aligned} P_G(h_i, g_j) &= \sum_{k=1}^n \mathbf{C}_{(i,k)} p(h_k, g_j) \\ &> \sum_{k=1}^n \mathbf{C}_{(i,k)} p(h_k, g_\ell) = P_G(h_i, g_\ell). \end{aligned} \quad (61)$$

Therefore, by using the information roadmap  $G$  to escape a local minimum  $\tilde{\mathbf{q}}_i \in h_i$ , the robotic sensor has a higher probability of converging to target  $\mathcal{T}_j$  than to  $\mathcal{T}_\ell$ , when  $V_j > V_\ell$ . This result is also demonstrated numerically in Section VI.

### E. Computational Complexity of Information Roadmap Method

The information roadmap method utilizes a local planner to verify the reachability of every milestone in the set  $M$ , under the switched-control law (25)–(31). Only reachable milestones in  $M$  are then used to construct  $G$ . If all pairs of milestones in  $M$  were considered by the planner, the number of iterations required would be  $\kappa(\kappa + 1)/2$ , where  $\kappa$  is the number of milestones added to  $M$  by the sampling process. However, it can be shown that the information roadmap method requires on average, a smaller number of iterations. Let  $r_i \geq 0$  denote the number of milestones added at the  $i$ th iteration of the information roadmap algorithm and  $T$  denote the last iteration. Then, it can be easily shown that  $T \leq \kappa$  and  $\sum_{i=1}^T r_i \leq \kappa$ . In the worst case, the number of iterations  $\tau$  is bounded as follows

$$\tau \leq \binom{\kappa}{2} - \sum_{i=1}^T \binom{r_i}{2} - \left( \kappa - \sum_{i=1}^T r_i \right) \quad (62)$$

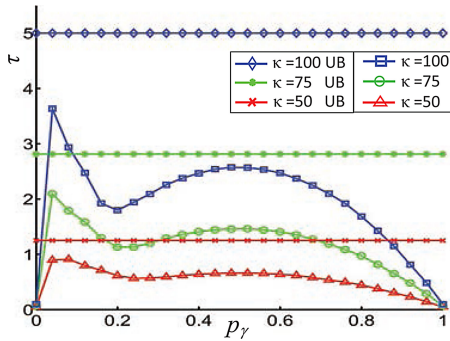


Fig. 7. Average number of iterations as a function of  $p_\gamma$  and comparison with corresponding UB  $\kappa(\kappa + 1)/2$ .

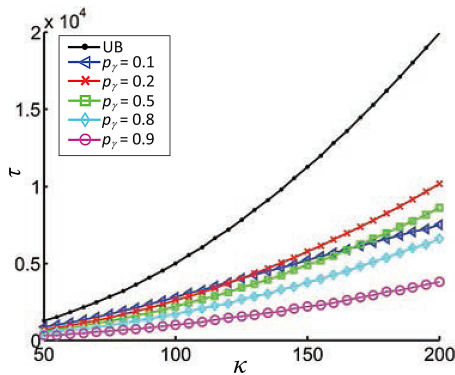


Fig. 8. Average number of iterations as a function of  $\kappa$  and comparison with corresponding UB  $\kappa(\kappa + 1)/2$ .

where for two scalar numbers  $n_1$  and  $n_2$

$$\binom{n_1}{n_2} = \frac{n_1!}{(n_1 - n_2)!n_2!} \quad (63)$$

denotes the binomial coefficient  $n_1$  choose  $n_2$ . If all milestones in  $M$  can be connected to  $\mathbf{m}_0$  at the first iteration, then  $T = 1$ ,  $r_1 = \kappa$ ,  $\tau = \kappa$ , and the computational complexity of the algorithm is  $O(\kappa)$ . When  $T = 1$  and  $r_1 = \delta\kappa$ , where  $0 < \delta < 1$ ,  $\tau = \kappa + \kappa^2(\delta - \delta^2)$ , and the computational complexity is  $O(\kappa^2)$ . Similarly, for  $T > 1$ , the computational complexity is still  $O(\kappa^2)$ , since, typically,  $r_i$  or  $\kappa - \sum_{i=1}^T r_i$  is much less than  $\kappa$ , and  $\kappa^2$  in (62) cannot be eliminated.

Although, in the worst case, the computational complexity has the same order as the UB  $\kappa(\kappa + 1)/2$ , the average value of  $\tau$  is less than UB. Average values of  $\tau$  as a function of the probability  $p_\gamma$  of finding a free path between two milestones  $\mathbf{m}_i$  and  $\mathbf{m}_l$  are computed using over 1000 simulations, and plotted in Figs. 7 and 8. It can be seen that for all chosen values of  $\kappa$ ,  $\tau$  achieves the highest value when  $p_\gamma < 0.1$ . For  $p_\gamma > 0.2$ , the highest value of  $\tau$ , obtained near  $p_\gamma = 0.5$ , is about half of UB. These results show that the average number of iterations is below 50% of UB for most values of the probability  $p_\gamma$ . Since the computational complexity of the algorithm is  $O(\kappa^2)$ , for large values of  $\kappa$ , the method can be too slow (see Fig. 8), especially for online applications. One way to further decrease  $\tau$  is to only verify reachability of the nearest milestones in  $M$ . However,

in this case, the information roadmap properties proven in the previous sections may no longer be guaranteed.

## V. ROBOTIC SENSOR SIMULATIONS

The IP method presented in the previous sections is demonstrated through a simulation environment developed using MATLAB<sup>®</sup>. All sensors are characterized by the geometric objects in Fig. 1 and their motion simulated by integrating the unicycle kinematics (1), with control inputs provided by the switched control law (25)–(31). The closed-loop kinematics are integrated using a fourth-order Runge–Kutta integration method [52], over a time interval  $[t_0, t_f]$ , with  $t_0 = 0$  (s) and  $t_f = 20$  (s). Additionally, to make the robot kinematics more realistic, the following bounds are simulated:  $|a| < 5$  (m/s<sup>2</sup>),  $|v| < 2$  (m/s), and  $|w| < \pi/10$  (rad/s<sup>2</sup>). Although these bounds are not accounted for explicitly by the unicycle model (1), it is shown in Section VI that the switched control law remains stable under these conditions.

The probabilistic model of sensor measurements (2) is a Bayesian network model of a ground-penetrating radar (GPR) taken from [36]. The target classification variable  $X$  is nonobservable and has two mutually exclusive values  $\mathcal{X} = \{x_1, x_2\}$ . The prior target PDF  $p_X(x_i)$  is given by prior measurements obtained by a simulated airborne Agema Thermovision 900 infrared (IR) sensor [17], [36]. The prior  $p_E(e_i)$  is assumed to be uniformly distributed over  $\mathcal{X}$ , and  $e_i$  is assumed known for all  $i = 1, \dots, M$ . When the sensor FOV  $\mathcal{S}$  intersects a target  $\mathcal{T}_i$ , the noisy measurement value  $z_i$  is obtained, and  $x_i$  is inferred from  $z_i$  using Bayes' rule in (3) and (4). Let  $N_{\text{IR}}$  denote the number of targets that are correctly classified by the IR sensor, prior to deploying the robotic GPR sensor, and let  $N_{\text{GPR}}$  denote the number of targets that are correctly classified after the GPR measurements have been obtained. Then

$$N_c = N_{\text{GPR}} - N_{\text{IR}} \quad (64)$$

represents the improvement in classification accuracy, or actual *classification performance*, of the robotic sensor.

The IP method presented in Section III is designed to account for the presence of other robotic sensors, which are considered as moving obstacles. A simple sensor-target assignment algorithm is used to assign targets to the sensors based on the distance between the  $i$ th target and the  $j$ th sensor

$$\rho_{ij} = \min_{\mathbf{q}' \in \mathcal{CT}_i} \|\mathbf{q}' - \mathbf{q}_j\| \quad (65)$$

where  $\mathbf{q}_j$  is the configuration of the  $j$ th robotic sensor. Then, the set of targets assigned to the  $j$ th sensor is  $\{\mathcal{T}_i \mid \rho_{ij} < \rho_{ik}, \forall k \neq j\}$ . The simulation terminates when all targets in  $\mathcal{W}$  are measured by at least one robotic sensor, or when  $t = t_f$ , whichever occurs first. At  $t_f$ , the distance traveled by a sensor is

$$D = \int_{t_0}^{t_f} [\dot{\mathbf{q}}(t)^T \dot{\mathbf{q}}(t)]^{1/2} dt. \quad (66)$$

Then, the overall robotic sensor efficiency, defined as the correct classification rate per unit distance, can be computed as follows

$$\eta = \frac{N_c}{D} \times 100. \quad (67)$$

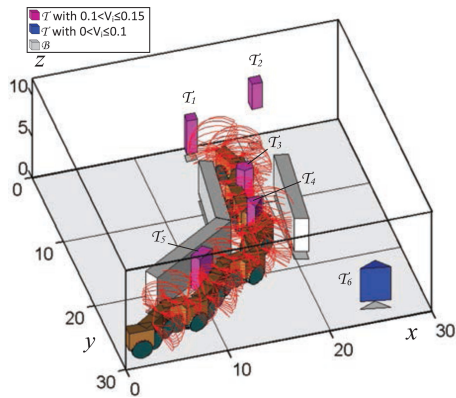


Fig. 9. Simulation results for one robotic sensor in a workspace with six targets, two obstacles, and one narrow passage.

The performance metrics  $N_c$ ,  $D$ , and  $\eta$  are used to evaluate the effectiveness of the IP method, and to compare IP to that of other path planning and control strategies.

## VI. SIMULATION RESULTS

The properties and effectiveness of the IP method are tested using a variety of workspaces obtained using the simulation in Section V. The simulation results show that the method is capable of controlling the robotic sensor in narrow passages, without oscillations, in order to enable measurements from targets located near obstacles. In addition, the IP method is shown effective at accounting for the location and geometry of the targets, and at avoiding collisions with other moving sensors based only on real-time position measurements. The closed-loop stability and properties of the IP method are verified in simulations, in the presence of multiple targets and obstacles, as well as control bounds. Then, the IP method is shown to outperform both the RRT method proposed [7] and a classical PF method that assigns a goal configuration to each target.

### A. Information Potential Sensor Path Planning and Control in Narrow Passages

The properties and effectiveness of the IP method are first illustrated using a workspace containing a narrow passage (see Fig. 9) and six targets, two of which ( $\mathcal{T}_3$  and  $\mathcal{T}_4$ ) are inside the narrow passage, and one of which ( $\mathcal{T}_5$ ) is near an obstacle. Targets with medium information value ( $0.1 < V_i \leq 0.15$ ) are shown in a magenta color and targets with low information value ( $0 < V_i \leq 0.1$ ) are shown in blue. This workspace is designed to test well-known issues of PF methods, such as 1) oscillations; 2) inability to enter narrow passages; and 3) goals nonreachable with obstacles nearby. As shown in Fig. 9, the IP method does not exhibit any of these limitations and allows the robot to enter narrow passages and obtain measurements from valuable targets despite their vicinity to obstacles. Other approaches for preventing these issues include adding a dampening force [53] or using a hybrid Voronoi diagram-visibility graph PF method [54].

The results in Fig. 9 also show that, in addition to maximizing target information value, the IP method considers the distance traveled to the targets. For example,  $\mathcal{T}_1$  and  $\mathcal{T}_2$ , with

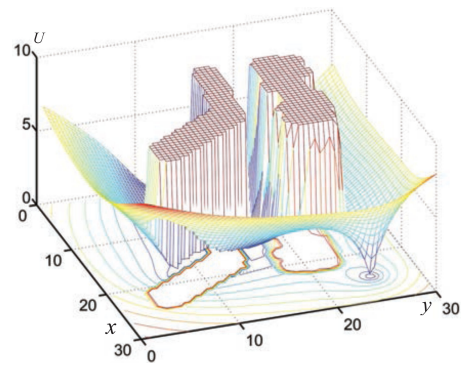


Fig. 10. Total IP for the example in Fig. 9.

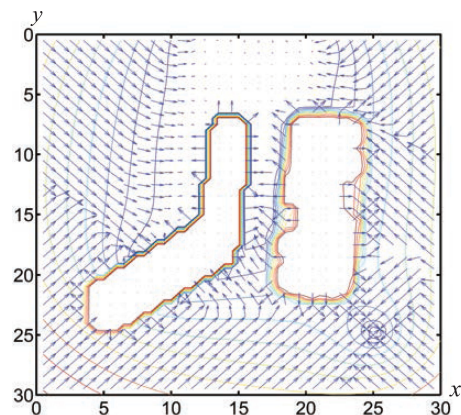


Fig. 11. Contour and gradient vector field for the IP in Fig. 10.

$V_1 = V_2 = 0.1314$ , have the same information value and geometry, but are at a different distance from the robot when it exits the narrow passage. Thus, in this case, the robotic sensor obtains measurements from  $\mathcal{T}_1$  because it is closer than  $\mathcal{T}_2$ . The results in Fig. 9 also show that the IP method allows the robotic sensor to obtain measurements from targets near obstacles without collisions, thanks to the IP plotted in Fig. 10, and further illustrated through a contour plot and gradient vector field in Fig. 11.

### B. Information Potential Multisensor Path Planning and Control in Narrow Passages

A workspace containing a narrow passage and two targets  $\mathcal{T}_1$  and  $\mathcal{T}_2$  (see Fig. 12) is used to illustrate that collisions with other robotic sensors can be avoided under the same challenging conditions used in Section VI-A. In this example, the two targets are assigned manually to two robotic sensors, forcing them to approach each other inside the narrow passage. The results show that IP allows the two robots to measure their assigned target, while avoiding a mutual collision, even when the two sensors are in the same narrow passage. Therefore, even near fixed obstacles ( $\mathcal{B}_1$  and  $\mathcal{B}_2$ ), the repulsive force defined in (16) is effective at avoiding collisions with moving obstacles online.

### C. Stability of Information Potential Switched Control Law

In Section IV-B, the IP switched control law (25)–(31) was proven to be closed-loop stable, under proper simplifying

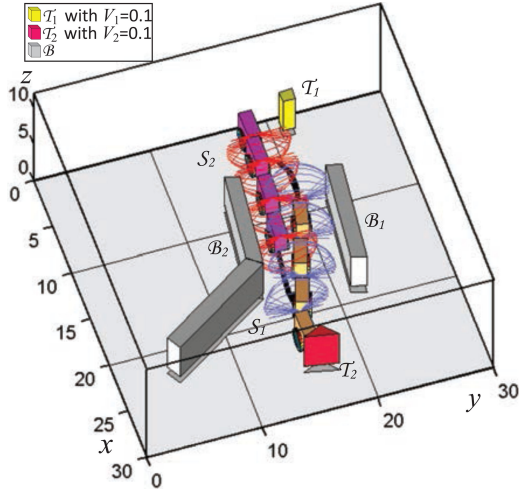


Fig. 12. Simulation results for two robotic sensors in a workspace with two targets, two obstacles, and one narrow passage.

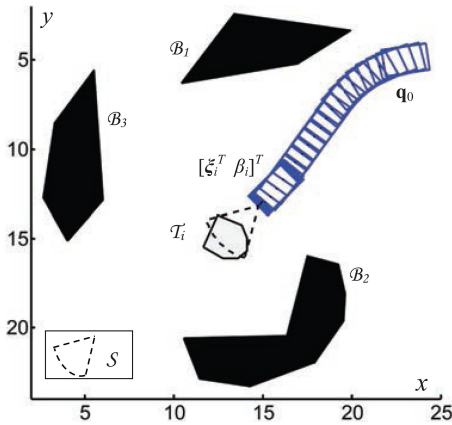


Fig. 13. Simulation results for a robotic sensor that converges to its goal configuration  $[\xi_i^T \beta_i]^T$ , for a target  $\mathcal{T}_i$  located near three obstacles,  $\mathcal{B}_1$ ,  $\mathcal{B}_2$ , and  $\mathcal{B}_3$ .

assumptions. Extensive numerical simulations showed that the IP switched control law remains stable even when these assumptions are violated, and the robotic sensor is subject to UBs on its linear acceleration  $a$ , linear velocity  $v$ , and angular velocity  $w$ . The effectiveness of IP when multiple targets are nearby, and assumption (II) is violated, is demonstrated in Sections VI-A and VI-B. The example in Fig. 13 is used to illustrate closed-loop stability for a target  $\mathcal{T}_i$  located near multiple obstacles  $\mathcal{B}_1$ ,  $\mathcal{B}_2$ , and  $\mathcal{B}_3$ , violating assumption (III), and for  $|a| < 5$  m/s<sup>2</sup>,  $|v| < 2$  m/s, and  $|w| < \pi/10$  rad/s. The path projected on the  $xy$ -plane in Fig. 13 shows that the robot converges from an initial configuration  $\mathbf{q}_0$ , to the goal configuration  $[\xi_i^T \beta_i]^T$  specified implicitly by the switched control law. As a result, the sensor is able to obtain measurements from the  $i$ th target when  $S \cap \mathcal{T}_i \neq \emptyset$ .

The variables used to design the switched control law (defined in Section III-B) are shown in Fig. 14, where the goal coordinates  $\xi_i$  are denoted by a star, and an example of sensor position  $\mathbf{x}$  is denoted by a cross. The arrows illustrate the robot orientation  $\theta$  and the goal orientation  $\beta_i$ . The time histories of the state and control inputs are plotted in Fig. 15, where  $t_\epsilon$  denotes the time

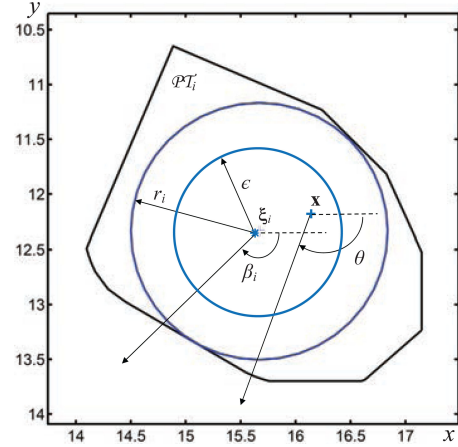


Fig. 14. Example of sensor configuration  $[\mathbf{x}^T \theta]$  and goal configuration  $[\xi_i^T \beta_i]$  for the path in Fig. 13.

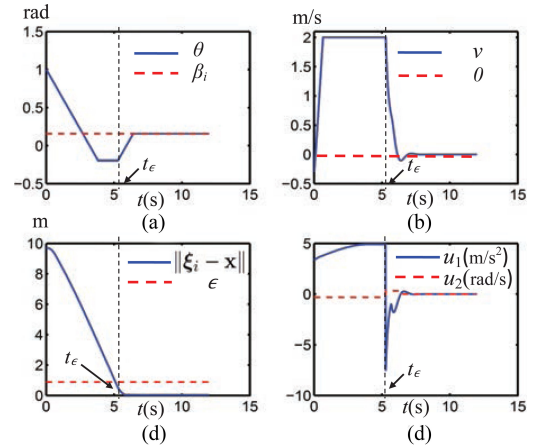


Fig. 15. Time histories of (a) sensor orientation, (b) linear velocity, (c) distance from C-target, and (d) control inputs, for the example in Fig. 13.

at which  $|\xi_i - \mathbf{x}| = \epsilon$ . These results confirm that, under the IP switched control law,  $\rho_i$ , defined in (24), goes to zero at  $t_\epsilon$ , and subsequently, for  $t > t_\epsilon$ ,  $\theta$  converges to  $\beta_i$ , and  $v$  goes to zero with a small overshoot so that the sensor remains inside the cylinder illustrated in Fig. 4.

#### D. Information Roadmap Method for Escaping Local Minima

The properties of the information roadmap method, derived in Sections IV-C and IV-D, are illustrated through the example in Fig. 16, containing one concave obstacle and two targets:  $\mathcal{T}_1$  with information value  $V_1 = 0.2$ , and  $\mathcal{T}_2$  with information  $V_2 = 0.1$ . The two targets are otherwise equivalent, because they are symmetrically positioned above and below the obstacle, and have the same geometry. The shape of the obstacle is chosen to create a local minimum in the potential function (see Fig. 17), causing the robot to be trapped at  $\tilde{\mathbf{q}}_i$ . Because  $U$  is characterized by a wider well around  $\mathcal{T}_1$ , the PDF  $f_{\mathbf{q}}$ , defined in (36), has higher values in  $CT_1$  than in  $CT_2$ , and thus configurations in  $CT_1$  have higher probability of being sampled than configurations in  $CT_2$ . From the set  $M$  of sampled configurations, a roadmap  $G$  containing a collision-free path from  $\tilde{\mathbf{q}}_i$  to  $CT_1$  is constructed

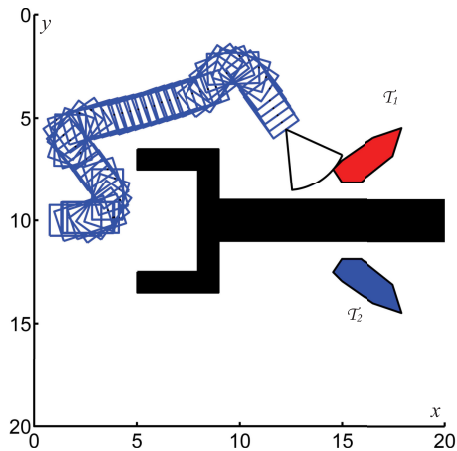


Fig. 16. Simulation results for a robotic sensor escaping a local minimum and converging to the target  $T_1$  with highest information value.

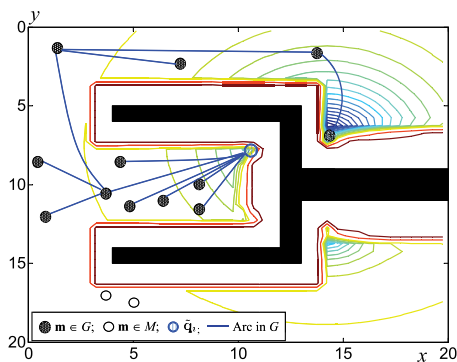


Fig. 17. IP contour for the example in Fig. 16 and information roadmap generated to escape local minimum.

(see Fig. 17), such that the robot can successfully escape  $\tilde{q}_i$  and obtain measurements from the most valuable target  $T_1$ .

### E. Performance Comparison

In this section, IP is compared to the RRT method proposed [7], as well as to a classical PF method that does not take into account target geometry and information value. Average values of classification performance (64), distance traveled (66), and sensor efficiency (67) are obtained by computing several paths and control laws for three sensors that are simultaneously deployed in five workspaces of the same size as the example in Fig. 18. The workspaces are obtained by first considering a medium obstacle density, coupled with a low ( $M = 15$ ), medium ( $M = 27$ ), or high ( $M = 40$ ) target density. Then, a medium target density is considered, coupled with a low ( $N = 10$ ), medium ( $N = 17$ ), or high ( $N = 24$ ) obstacle density. For every simulation, the positions and geometries of the targets and obstacles are generated randomly, as are the initial configurations of the robotic sensors, and the information value of the targets.

The average sensor efficiency obtained by IP is summarized in Table I. It can be seen that for the same obstacle density, the sensor performance increases when the target density increases, because more targets can be classified per unit distance. In addition, as can be expected, for the same target density, the sensor

TABLE I  
AVERAGE EFFICIENCY OF THE IP METHOD

Obstacle density	Target density	$\bar{\eta}$
Medium	Low	0.0223
Medium	Medium	0.0240
Medium	High	0.0482
Low	Medium	0.0439
High	Medium	0.0148

TABLE II  
AVERAGE PERFORMANCE COMPARISON FOR  $M = 27$

Obstacle density	Performance	IP	RRT	PF
Low	$\bar{\eta}$	.0439	.0143	.0126
	$D$	296.6	420	318
	$N_c$	13	6	4
Medium	$\bar{\eta}$	.024	.0139	.0132
	$D$	513	397	190
	$N_c$	12.3	5.5	2.5
High	$\bar{\eta}$	.0148	.0043	.0055
	$D$	575	460	109.5
	$N_c$	8.5	2	0.6

performance increases when the obstacle density decreases, because the sensor can travel a shorter distance to reach the same targets. One interesting outcome is that the efficiency does not increase significantly when the target density increases from low to medium (for a medium obstacle density), because a higher target density also requires the sensor to travel farther and, possibly, inside narrow passages.

In Table II, the performance of IP is compared to the performance of classic PF and RRT. It can be seen that sensors controlled by IP outperform sensors controlled by PF and RRT not only in average sensor efficiency ( $\bar{\eta}$ ), but also in the number of targets correctly classified ( $N_c$ ), under all conditions examined. On the other hand, as can be expected, the distance traveled ( $D$ ) by IP-controlled sensors may be higher than that of sensors controlled by PF, because with IP the sensors travel to find targets of high information value. Typically, IP leads to lower values of  $D$  than RRT, because IP allows the robotic sensors to avoid unnecessary routes, and produces smoother paths. However, when the obstacle density is high,  $D$  may be higher for IP because with IP the sensors move to obtain measurements from approximately 75% of their assigned targets, while RRT typically measures only 50% of the targets. As can be expected, classic PF displays the worse classification performance because it does not take into account the target information value in planning the robotic sensor path.

An example of sensor paths obtained by IP in a workspace with medium target and obstacle densities is shown in Fig. 18. It can be seen from Fig. 19 that when the RRT method is implemented in the same workspace, the paths are not as smooth as with IP, and a smaller percentage of valuable targets is measured by the sensors. In the simulations, it was found that the classic PF method typically measures a smaller percentage of assigned targets than RRT, because the sensors are easily trapped in local minima, as shown in Fig. 21. As a result, PF exhibits the shortest distance traveled and the smallest number of targets properly

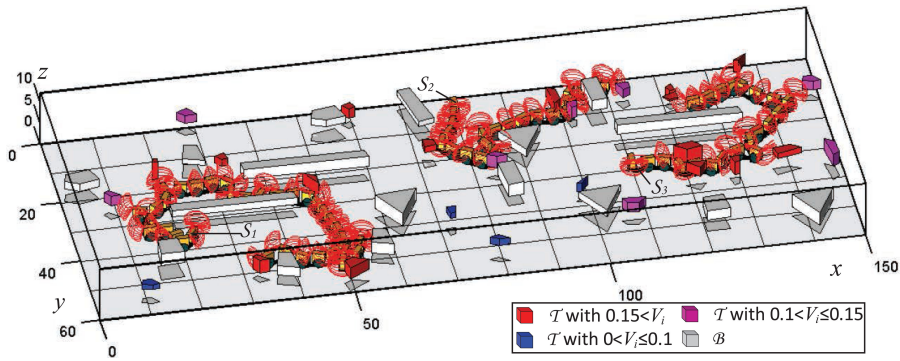


Fig. 18. Example of sensor paths obtained by IP for three sensors deployed in a workspace with  $N = 17$  obstacles and  $M = 27$  targets.

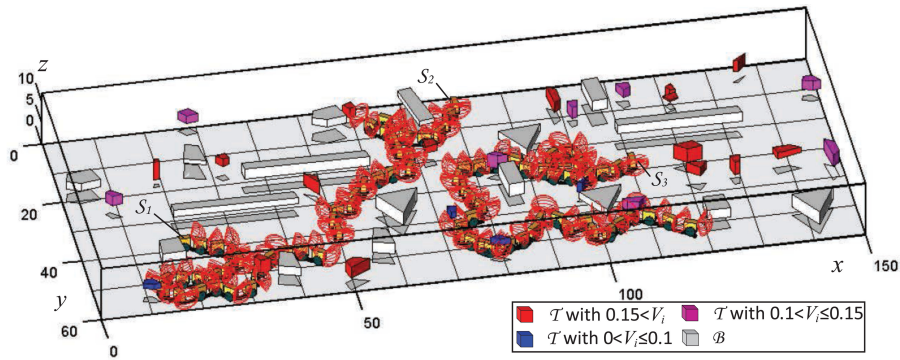


Fig. 19. Example of sensor paths obtained by RRT in the same workspace used in Fig. 18.

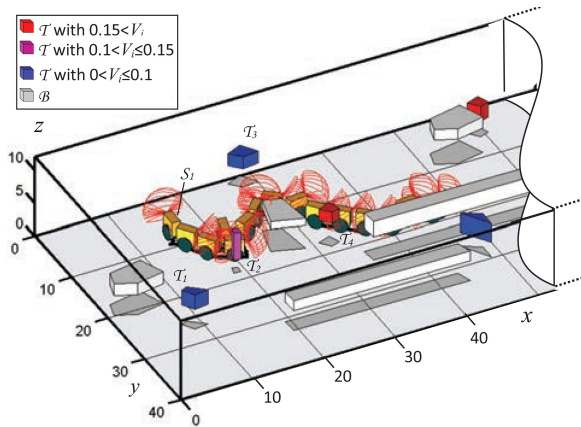


Fig. 20. Detail of sensor path obtained by the IP method.

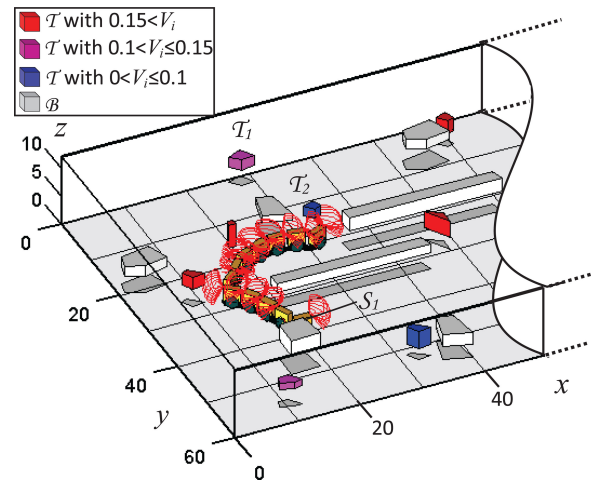


Fig. 21. Detail of sensor path obtained by the classic PF method.

classified for any conditions (see Table II). Furthermore, when the obstacle density is high, PF exhibits the shortest distance traveled (see Table II), because the higher the obstacle density, the higher the probability of a sensor becoming trapped in a local minimum. Finally, from Fig. 20, it can be seen that through the new attractive potential function in (11), IP allows the sensor to favor targets with higher information value. For example, in Fig. 20, the IP-controlled robotic sensor measures  $\mathcal{T}_2$  instead of  $\mathcal{T}_1$ , and  $\mathcal{T}_4$  instead of  $\mathcal{T}_3$ , despite each pair being at a similar distance from the sensor path. On the other hand, as shown in

Fig. 21, the PF-controlled sensor measures  $\mathcal{T}_2$  instead of  $\mathcal{T}_1$ , despite  $\mathcal{T}_1$  being the target of the highest information value.

#### F. Information Potential Performance Analysis

This section analyzes the influence of the number of robots and prior measurements on the performance of the IP method. Eighty workspaces with the same dimensions as the one shown in Fig. 18, medium target and obstacle density, and up to  $L = 8$  robots, are simulated. The average performance metrics of each

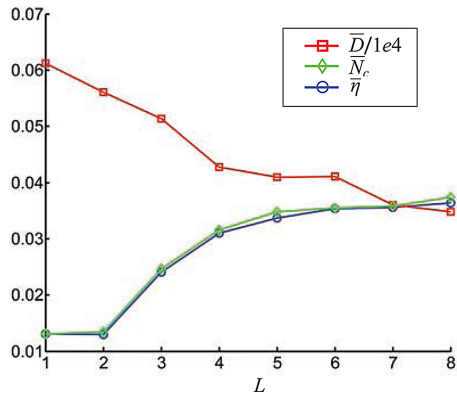


Fig. 22. Average distance traveled, classification performance, and efficiency as a function of the number of sensors in  $\mathcal{W}$ .

TABLE III  
TARGET INFORMATION INFLUENCE ON PERFORMANCE

Performance \ Method	IP	IP <sub>1</sub>	IP <sub>2</sub>
$\eta$	0.024	0.0098	0.0046
$D$	513	813	1085
$N_c$	12	8	5

sensor are plotted as a function of  $L$  in Fig. 22. It can be seen that all metrics rapidly improve as  $L$  increases above 1, and then come to a plateau around  $L = 7$ , due to the size of the workspace. Thus, the IP method allows multiple robotic sensors to operate efficiently, while avoiding mutual collisions. In order to illustrate the influence of prior measurements on IP performance, the IP method is also implemented using targets with the same information value  $V_i$  for all  $i \in I_T$  (IP<sub>1</sub>), and then with no knowledge of the targets (IP<sub>2</sub>). The results in Table III show that, by accounting for prior target information, the sensor efficiency can be improved by as much as 422%, compared with when no target information is utilized.

## VII. CONCLUSION

This paper presents an IP method for integrated sensor path planning and control in obstacle-populated environments. The method is based on a potential function defined from conditional mutual information that is used to design a switched feedback control law, as well as to generate a local PRM for escaping local minima, while obtaining valuable sensor measurements. This paper proves several properties of the IP method, including closed-loop stability. Numerical simulations verify that the method takes advantage of online obstacle avoidance, prior target information, and coordination among robotic sensors, and that it outperforms existing strategies, such as RRTs and a modified PF method.

## APPENDIX

$\mathbf{M} =$

$$\begin{bmatrix} p(g_1, g_1) & \cdots & p(g_1, g_m) & p(g_1, h_1) & \cdots & p(g_1, h_n) \\ \vdots & \ddots & \vdots & \vdots & \ddots & \vdots \\ p(g_m, g_1) & \cdots & p(g_m, g_m) & p(g_m, h_1) & \cdots & p(g_m, h_n) \\ p(h_1, g_1) & \cdots & p(h_1, g_m) & p(h_1, h_1) & \cdots & p(h_1, h_n) \\ \vdots & \ddots & \vdots & \vdots & \ddots & \vdots \\ p(h_n, g_1) & \cdots & p(h_n, g_m) & p(h_n, h_1) & \cdots & p(h_n, h_n) \end{bmatrix} \quad (68)$$

## REFERENCES

- [1] R. Siegel, "Land mine detection," *IEEE Instrum. Meas. Mag.*, vol. 5, no. 4, pp. 22–28, Dec. 2002.
- [2] C. Hofner and G. Schmidt, "Path planning and guidance techniques for an autonomous mobile cleaning robot," *Robot. Auton. Syst.*, vol. 14, pp. 199–212, 1995.
- [3] S. Ferrari, C. Cai, R. Fierro, and B. Perteet, "A multi-objective optimization approach to detecting and tracking dynamic targets in pursuit-evasion games," in *Proc. Am. Control Conf.*, New York, NY, USA, 2007, pp. 5316–5321.
- [4] D. Culler, D. Estrin, and M. Srivastava, "Overview of sensor networks," *Computer*, vol. 37, no. 8, pp. 41–49, 2004.
- [5] A. Censi and R. Murray, "Learning diffeomorphism models of robotic sensorimotor cascades," presented at the IEEE Int. Conf. Robot. Autom., Minnesota, MN, USA, 2012.
- [6] C. Cai and S. Ferrari, "Information-driven sensor path planning by approximate cell decomposition," *IEEE Trans. Syst., Man, Cybern. B, Cybern.*, vol. 39, no. 3, pp. 672–689, Jun. 2009.
- [7] W. Lu, G. Zhang, and S. Ferrari, "A randomized hybrid system approach to coordinated robotic sensor planning," in *Proc. IEEE Conf. Decision Control*, 2010, pp. 3857–3864.
- [8] S. Ponda, N. Ahmed, B. Luders, E. Sample, T. Hoossainy, D. Shah, M. Campbell, and J. How, "Decentralized information-rich planning and hybrid sensor fusion for uncertainty reduction in human-robot missions," in *Proc. AIAA Guid., Navigat., Control Conf.*, Portland, OR, USA, Aug. 2011, pp. 8–11.
- [9] K. Yang, S. K. Gan, and S. Sukkarieh, "An efficient path planning and control algorithm for RUAV in unknown and cluttered environments," *J. Intell. Robot. Syst.*, vol. 57, no. 1–4, pp. 101–122, 2010.
- [10] G. M. Hoffmann and C. J. Tomlin, "Mobile sensor network control using mutual information methods and particle filters," *IEEE Trans. Autom. Control*, vol. 55, no. 1, pp. 32–47, Jan. 2010.
- [11] M. Chu, H. Haussecker, and F. Zhao, "Scalable information-driven sensor querying and routing for Ad Hoc heterogeneous sensor networks," *Int. J. High Perform. Comput. Appl.*, vol. 16, no. 3, pp. 293–313, 2002.
- [12] F. Zhao, J. Shin, and J. Reich, "Information-driven dynamic sensor collaboration," *IEEE Signal Process. Mag.*, vol. 19, no. 2, pp. 61–72, Mar. 2002.
- [13] A. Censi, L. Marchionni, and G. Oriolo, "Simultaneous maximum-likelihood calibration of odometry and sensor parameters," in *Proc. IEEE Int. Conf. Robot. Autom.*, 2008, pp. 2098–2103.
- [14] K. M. Lynch, I. B. Schwartz, P. Yang, and R. A. Freeman, "Decentralized environmental modeling by mobile sensor networks," *IEEE Trans. Robot.*, vol. 24, no. 3, pp. 710–724, Jun. 2008.
- [15] N. Mansard and F. Chaumette, "Task sequencing for high-level sensor-based control," *IEEE Trans. Robot.*, vol. 23, no. 1, pp. 60–72, Feb. 2007.
- [16] H. Zhou and S. Sakane, "Sensor planning for mobile robot localization—A hierarchical approach using a Bayesian network and a particle filter," *IEEE Trans. Robot.*, vol. 24, no. 2, pp. 481–487, Apr. 2008.
- [17] G. Zhang, S. Ferrari, and M. Qian, "An information roadmap method for robotic sensor path planning," *J. Intell. Robot. Syst.*, vol. 56, pp. 69–98, 2009.
- [18] S. Ferrari and C. Cai, "Information-driven search strategies in the board game of CLUE," *IEEE Trans. Syst., Man, Cybern. B, Cybern.*, vol. 39, no. 3, pp. 607–625, Jun. 2009.

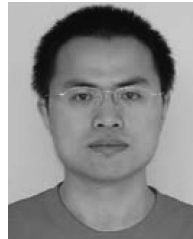
- [19] G. Zhang, S. Ferrari, and C. Cai, "A comparison of information functions and search strategies for sensor planning in target classification," *IEEE Trans. Syst., Man, Cybern. B, Cybern.*, vol. 42, no. 1, pp. 2–16, Feb. 2012.
- [20] N. S. V. Rao, "Robot navigation in unknown generalized polygonal terrains using vision sensors," *IEEE Trans. Syst., Man, Cybern.*, vol. 25, no. 6, pp. 947–962, Jun. 1995.
- [21] K. Song and C. C. Chang, "Reactive navigation in dynamic environment using a multisensor predictor," *IEEE Trans. Syst., Man, Cybern. B, Cybern.*, vol. 29, no. 6, pp. 870–880, Dec. 1999.
- [22] M. Kazemi, M. Mehrandezh, and K. Gupta, "Sensor-based robot path planning using harmonic function-based probabilistic roadmaps," in *Proc. 12th Int. Conf. Adv. Robot.*, 2005, pp. 84–89.
- [23] Z. Sun and J. H. Reif, "On robotic optimal path planning in polygonal regions with pseudo-Euclidean metrics," *IEEE Trans. Syst., Man, Cybern. A, Cybern.*, vol. 37, no. 4, pp. 925–936, Aug. 2007.
- [24] X.-C. Lai, S.-S. Ge, and A. Al-Mamun, "Hierarchical incremental path planning and situation-dependent optimized dynamic motion planning considering accelerations," *IEEE Trans. Syst., Man, Cybern. A, Cybern.*, vol. 37, no. 6, pp. 1541–1554, Dec. 2007.
- [25] Y. Koren and J. Borenstein, "Potential field methods and their inherent limitations for mobile robot navigation," in *Proc. IEEE Conf. Robot. Autom.*, Sacramento, CA, USA, 1991, pp. 1398–1404.
- [26] C. Samson, "Time-varying feedback stabilization of car-like wheeled mobile robots," *Int. J. Robot. Res.*, vol. 12, no. 1, pp. 55–64, 1993.
- [27] A. Astolfi, "On the stabilization of nonholonomic systems," in *Proc. IEEE Conf. Decision Control*, 1994, pp. 3481–3486.
- [28] K. D. Do, Z.-P. Jiang, and J. Pan, "A global output-feedback controller for simultaneous tracking and stabilization of unicycle-type mobile robots," *IEEE Trans. Robot. Autom.*, vol. 20, no. 3, pp. 589–594, Jun. 2004.
- [29] A. Bloch, M. Reyhanoglu, and N. McClamroch, "Control and stabilization of nonholonomic dynamic systems," *IEEE Trans. Autom. Control*, vol. 37, no. 11, pp. 1746–1757, Nov. 1992.
- [30] K. Pathak and S. K. Agrawal, "An integrated path-planning and control approach for nonholonomic unicycles using switched local potentials," *IEEE Trans. Robot.*, vol. 21, no. 6, pp. 1201–1208, Dec. 2005.
- [31] B. Girau and A. Boumaza, "Embedded harmonic control for dynamic trajectory planning on FPGA," in *Proc. Int. Conf. Artif. Intell. Appl.*, Innsbruck, Australia, 2007, pp. 244–249.
- [32] S. Waydo and R. M. Murray, "Vehicle motion planning using stream functions," in *Proc. IEEE Int. Conf. Robot. Autom.*, Taipei, Taiwan, 2003, pp. 2484–2491.
- [33] J. Rosell and P. Iniguez, "Path planning using harmonic functions and probabilistic cell decomposition," in *Proc. IEEE Int. Conf. Robot. Autom.*, Barcelona, Spain, 2005, pp. 1815–1820.
- [34] A. Masoud, "A harmonic potential approach for simultaneous planning and control of a generic UAV platform," *J. Intell. Robot. Syst.*, vol. 65, no. 1–4, pp. 153–173, 2012.
- [35] S. M. LaValle, *Planning Algorithms*. Cambridge, U.K.: Cambridge Univ. Press, 2006. [Online]. Available <http://planning.cs.uiuc.edu/>.
- [36] S. Ferrari and A. Vaghi, "Demining sensor modeling and feature-level fusion by Bayesian networks," *IEEE Sens.*, vol. 6, no. 2, pp. 471–483, Apr. 2006.
- [37] C. Kreucher, K. Kastella, and A. Hero, "Sensor management using an active sensing approach," *Signal Process.*, vol. 85, pp. 607–624, 2005.
- [38] C. Cai, S. Ferrari, and Q. Ming, "Bayesian network modeling of acoustic sensor measurements," in *Proc. IEEE Sens.*, Atlanta, GA, USA, 2007, pp. 345–348.
- [39] D. Pfeiffer and U. Franke, "Efficient representation of traffic scenes by means of dynamic stixels," in *Proc. IEEE Intell. Veh. Symp. (IV)*, Jun. 2010, pp. 217–224.
- [40] J. C. Latombe, *Robot Motion Planning*. Norwell, MA, USA: Kluwer, 1991.
- [41] A. Dumitrescu, A. Ebbens-Baumann, A. Grüne, R. Klein, and G. Rote, "On the geometric dilation of closed curves, graphs, and point sets," *Comput. Geom.*, vol. 36, no. 1, pp. 16–38, 2007.
- [42] L. Eriksson, M. Allie, and R. Greiner, "The selection and application of an IIR adaptive filter for use in active sound attenuation," *IEEE Trans. Acoust., Speech Signal Process.*, vol. 35, no. 4, pp. 433–437, Apr. 1987.
- [43] L. E. Kavradi, P. Svetska, J.-C. Latombe, and M. H. Overmars, "Probabilistic roadmaps for path planning in high-dimensional configuration space," *IEEE Trans. Robot. Autom.*, vol. 12, no. 4, pp. 566–580, Aug. 1996.
- [44] G. Casella and R. Berger, *Statistical Inference*. Pacific Grove, CA, USA: Duxbury, 2001.
- [45] S. S. Ge and Y. J. Cui, "New potential functions for mobile robot path planning," *IEEE Trans. Robot. Autom.*, vol. 16, no. 5, pp. 615–620, Oct. 2000.
- [46] T. M. Cover and J. A. Thomas, *Elements of Information Theory*. New York, NY, USA: Wiley, 1991.
- [47] H. Khalil, *Nonlinear Systems*. Englewood Cliffs, NJ, USA: Prentice-Hall, 2002.
- [48] F. Lamiraux and J. P. Laumond, "On the expected complexity of random path planning," in *Proc. IEEE Int. Conf. Robot. Autom.*, 1996, pp. 3306–3311.
- [49] R. S. Varga, *Matrix Iterative Analysis*. New York, NY, USA: Springer-Verlag, 1962.
- [50] G. W. Stewart, "Gershgorin theory for the generalized eigenvalue problem  $ax = \lambda bx$ ," *Math. Comput.*, vol. 29, no. 130, pp. 600–606, 1975.
- [51] G. F. Lawler, *Introduction to Stochastic Processes*. Boca Raton, FL, USA: Chapman & Hall/CRC, 2006.
- [52] S. M. LaValle and J. J. Kuffner, "Randomized kinodynamic planning," *Int. J. Robot. Res.*, vol. 20, no. 5, pp. 378–400, 2001.
- [53] A. A. Masoud, "Solving the narrow corridor problem in potential field-guided autonomous robots," in *Proc. IEEE Int. Conf. Robot. Autom.*, Apr. 2005, pp. 2909–2914.
- [54] E. Masehian and M. R. Amin-Naseri, "A Voronoi diagram-visibility graph-potential field compound algorithm for robot path planning," *J. Robot. Syst.*, vol. 21, no. 6, pp. 275–300, 2004.



**Wenjie Lu** received the M.S. degree in mechanical engineering from Duke University, Durham, NC, USA, in 2011, and the B.S. degree in mechatronics engineering from Zhejiang University, Hangzhou, Zhejiang, China, in 2009. He is currently working toward the Ph.D. degree in mechanical engineering at Duke University.

His research interests include intelligent mobile sensor agent that can adapt to heterogeneous environmental conditions, approximate dynamic programming, hybrid systems, information theory, and

nonparametric Bayesian models.



**Guoxian Zhang** received the B.S. and M.S. degrees from Tsinghua University, Beijing, China, in 2003 and 2006, respectively, and the Ph.D. degree from Duke University, Durham, NC, USA, in 2010.

He is currently a Data Scientist with Groupon, Inc., Palo Alto, CA, USA. His current research interests include robot and sensor path planning, data mining, multiagent systems, big data analysis, Bayesian statistics, and decision making under uncertainty.

Dr. Zhang has been a member of the American Society of Mechanical Engineers since 2008.



**Silvia Ferrari** (SM'13) received the B.S. degree from Embry-Riddle Aeronautical University, Daytona Beach, FL, USA, and the M.A. and Ph.D. degrees from Princeton University, Princeton, NJ, USA.

She is currently a Professor of engineering and computer science and the director of the Laboratory for Intelligent Systems and Controls at Duke University, Durham, NC, USA. She is a member of the Duke Institute for Brain Sciences and the information initiative at Duke. Her principal research interests include information-driven planning and control, learning and approximate dynamic programming, and distributed optimal control.

Dr. Ferrari received the Office of Naval Research Young Investigator Award in 2004, the National Science Foundation CAREER Award in 2005, and the Presidential Early Career Award for Scientists and Engineers in 2006. She is a member of the American Society of Mechanical Engineers, the International Society for Optical Engineers, and the American Institute of Aeronautics and Astronautics.